Clouds, Precipitation, and Marine Boundary Layer Structure during the MAGIC Field Campaign

XIAOLI ZHOU AND PAVLOS KOLLIAS

Department of Atmospheric and Oceanic Sciences, McGill University, Montreal, Quebec, Canada

ERNIE R. LEWIS

Biological, Environmental and Climate Sciences Department, Brookhaven National Laboratory, Upton, New York

(Manuscript received 2 May 2014, in final form 16 December 2014)

ABSTRACT

The recent ship-based Marine ARM GCSS Pacific Cross-Section Intercomparison (GPCI) Investigation of Clouds (MAGIC) field campaign with the marine-capable Second ARM Mobile Facility (AMF2) deployed on the Horizon Lines cargo container M/V *Spirit* provided nearly 200 days of intraseasonal high-resolution observations of clouds, precipitation, and marine boundary layer (MBL) structure on multiple legs between Los Angeles, California, and Honolulu, Hawaii. During the deployment, MBL clouds exhibited a much higher frequency of occurrence than other cloud types and occurred more often in the warm season than in the cold season. MBL clouds demonstrated a propensity to produce precipitation, which often evaporated before reaching the ocean surface. The formation of stratocumulus is strongly correlated to a shallow MBL with a strong inversion and a weak transition, while cumulus formation is associated with a much weaker inversion and stronger transition. The estimated inversion strength is shown to depend seasonally on the potential temperature at 700 hPa. The location of the commencement of systematic MBL decoupling always occurred eastward of the locations of cloud breakup, and the systematic decoupling showed a strong moisture stratification. The entrainment of the dry warm air above the inversion appears to be the dominant factor triggering the systematic decoupling, while surface latent heat flux, precipitation, and diurnal circulation did not play major roles. MBL clouds broke up over a short spatial region due to the changes in the synoptic conditions, implying that in real atmospheric conditions the MBL clouds do not have enough time to evolve as in the idealized models.

1. Introduction

On average, near 30% of the global oceans are covered with low-level clouds [see the International Satellite Cloud Climatology Project (ISCCP) online dataset, at http://isccp.giss.nasa.gov/climanal7.html]. These prevailing marine boundary layer (MBL) clouds are a key component in Earth's radiation budget, from which stratocumulus (Sc) clouds exert a strong negative net radiative effect due to their low height and high areal coverage, by strongly reflecting incoming solar radiation but only weakly influencing the outgoing longwave radiation (Wood 2012). Cumulus (Cu) have a reduced effect on the radiation due to their low areal coverage (Wood 2012; Karlsson et al. 2010) but play a critical role in the vertical redistribution of moisture and energy in the lower troposphere (Tiedtke et al. 1988). Thus, it is important for global climate models to accurately represent these cloud regimes.

The evolution, with increasing sea surface temperature (SST), from Sc regimes to Cu regimes in the trade wind regions and then eventually to congestus and deep convective Cu over the warmer waters of the intertropical convergence zone is well documented (e.g., Albrecht et al. 1995a,b; Karlsson et al. 2010). An inversion layer that is often thought of as the top of the MBL typically caps the Sc. A regime with Cu under Sc usually occurs during the progression between Sc and Cu and is associated with a weakly stable layer below the inversion base that is characterized by a sharp decrease of moisture with height (e.g., Krueger et al. 1995; Bretherton and Wyant

Corresponding author address: Xiaoli Zhou, Department of Atmospheric and Oceanic Sciences, Burnside Hall, Room 945, 805 Sherbrooke Street West, Montreal QC H3A0B9, Canada.
E-mail: xiaoli.zhou@mail.mcgill.ca

DOI: 10.1175/JCLI-D-14-00320.1

1997; Jones et al. 2011). This stable layer, referred here as the transition layer, separates a region below of surface flux–driven turbulence from a region above dominated by radiatively driven convection (Bretherton and Wyant 1997) and acts to isolate the upper MBL from the surface moisture supply. When this vertical moisture stratification gets sufficiently strong, systematic decoupling occurs and the MBL remains decoupled with further increase in SST. This systematic decoupling is a crucial first step in the Sc-to-Cu transition and is not affected by the diurnal cycle of radiation (Wyant et al. 1997).

Because of the lack of full understanding of the mechanisms responsible for the evolution of MBL structure and clouds, global weather and climate prediction models still do not accurately reproduce the evolution between these cloud regimes, and the locations of Sc breakup and the rates of change of cloud coverage vary widely among different models, which generally underestimate cloud amounts in the Sc region while overestimating them in the Cu region (Teixeira et al. 2011).

One of the main factors hindering progress in representing these clouds in numerical models has been the lack of observational data. Most of the observational datasets used to evaluate the cloud-related processes are satellite based. Satellite data have proven valuable in determining the climatological links between MBL inversion base height (MBLH) and cloud cover (e.g., Heck et al. 1990; Wang et al. 1993; Wood and Bretherton 2004). However, satellite observations cannot provide information on detailed vertical cloud and thermodynamic structure of the MBL especially during decoupling conditions (Wood and Bretherton 2004; Karlsson et al. 2010). The difficulty in accurately observing low-level clouds with small-scale variability (Xu and Cheng 2013) further restricts the applicability of satellite data in the understanding of the transition between these cloud regimes.

In addition to satellite data, several field campaigns have been conducted to study MBL clouds and the mechanisms responsible for the Sc-to-Cu transition. These previous ship- or aircraft-based efforts provided a wealth of information with regard to the vertical structure of the MBL and associated clouds. However, they were primarily conducted in a fairly small region and focused on studying one specific cloud type. For example, the First ISCCP Regional Experiment (FIRE; Albrecht et al. 1988) focused on Sc and cirrus cloud regimes; the Tropical Instability Wave Experiment (TIWE; Albrecht et al. 1995b) focused on the trade wind Cu boundary layer structure; and during the Atlantic Stratocumulus Transition Experiment (ASTEX; Albrecht et al. 1995a) a transition region in which Cu form beneath Sc was observed. Albrecht et al. (1995b) compared the large-scale forcing and thermodynamic profiles from these three field experiments and concluded that the increase in SST is important in the thinning of the Sc. The same study provided evidence that the boundary layer structure and the associated transition from Sc to Cu may be more complicated than originally thought. More recently, Jones et al. (2011) examined in detail the coupled and decoupled boundary layers in the Variability of the American Monsoon Systems (VAMOS) Ocean–Cloud–Atmosphere–Land Study Regional Experiment (VOCALS-REx; Wood et al. 2011). One of the major findings in Jones et al. (2011) is that the difference between MBLH and the lifting condensation level (LCL) best predicts decoupling.

Previous numerical studies have demonstrated that the systematic decoupling is mainly driven by the increasing surface latent heat flux (LHF) as a response to the increasing entrainment due to the warmer SST (e.g., Bretherton and Wyant 1997; Sandu and Stevens 2011). The subsequent Sc breakup was explained as a result of the further increase of the SST that causes the Cu to become deeper and more vigorous, penetrating farther into the inversion and entraining more dry air from above the inversion (Wyant et al. 1997; Sandu and Stevens 2011). Although numerical studies have advanced our knowledge of MBL structure and clouds, simulations have usually simplified the problem by assuming the constant divergence and free-tropospheric lapse rates (Bretherton and Wyant 1997), but neither assumption is supported by observations.

There are noticeable discrepancies between idealized model simulations and observational findings. For instance, the dominant effect of the LHF on MBL decoupling was not observed in VOCAL-REx (Jones et al. 2011). Additionally, the assumption of a constant free-atmosphere lapse rate might introduce biases because MBLH and boundary layer mixing ratios are very sensitive to above-inversion features (Albrecht 1984; Krueger et al. 1995). At the same time, the availability of comprehensive, long-term observations that document the gradual MBL decoupling and Sc-to-Cu transitions is limited.

The recent Marine ARM GCSS Pacific Cross-Section Intercomparison (GPCI) Investigation of Clouds (MAGIC) field campaign provided high-resolution profiling observations from the coast of California to Honolulu for over 200 days. The collected dataset is the most extensive direct, long-term, intraseasonal set of measurements of MBL structure and cloud evolution from Sc to Cu over large downwind regions. Here, we investigate the potential of the dataset in advancing our understanding of the systematic MBL decoupling and Sc breakup to be compared with and constrain the modeling studies.

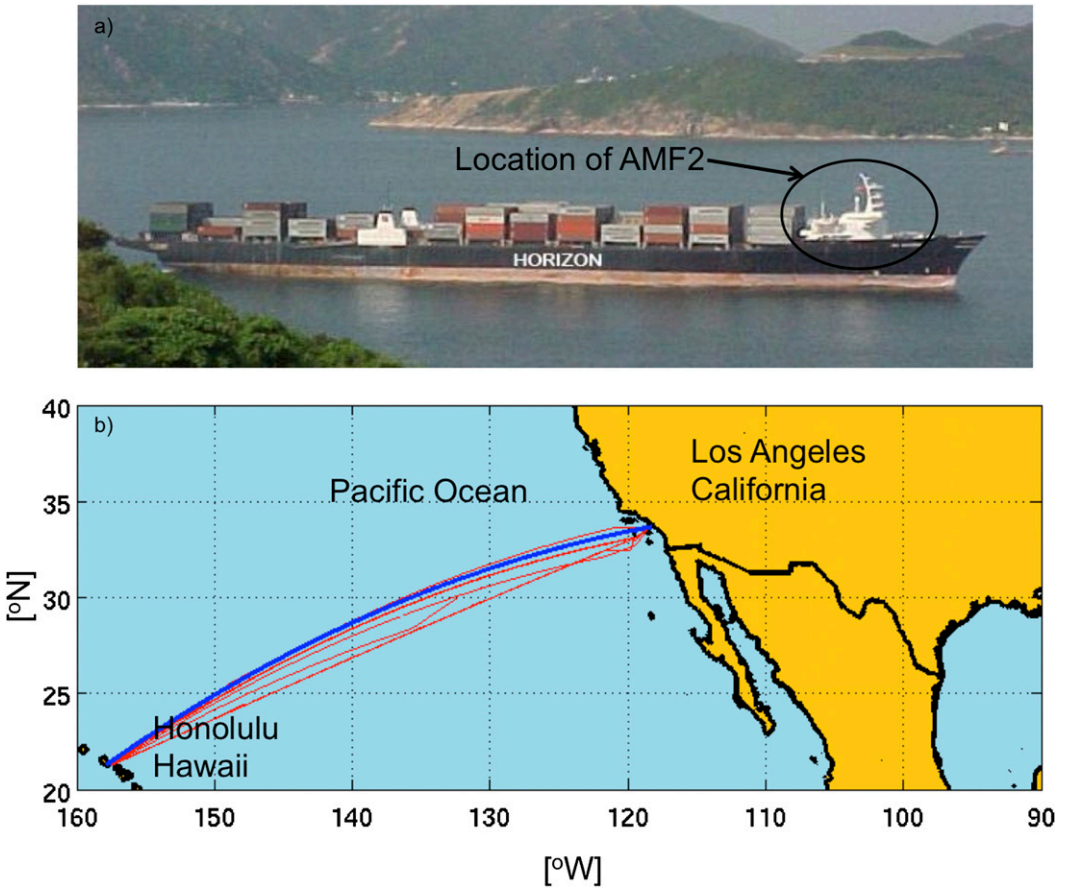

FIG. 1. (a) Horizon *Spirit* showing location of the bridge region where the AMF2 was located. (b) Tracks of MAGIC legs between California and Hawaii (red lines) and great circle route (blue line).

The remainder of the manuscript is organized as follows. Brief descriptions of the MAGIC field campaign and of the Second ARM Mobile Facility (AMF2) instruments are provided in section 2, and the methodology used for this study is introduced in section 3. Results are presented in section 4, and a summary of these results and plans for future work are presented in section 5.

2. Observations

a. The MAGIC field campaign

The MAGIC field campaign (http://www.arm.gov/sites/amf/mag/) deployed the U.S. Department of Energy (DOE) Atmospheric Radiation Measurement Program Mobile Facility 2 (AMF2) on the commercial cargo container ship Horizon *Spirit* (Fig. 1a). The MAGIC transect is very near the line from the coast of California to the equator (35°N, 125°W to 1°S, 173°W) that was chosen by modelers to compare model results for the Global Energy and Water Experiment (GEWEX) Cloud System Studies (GCSS) Pacific Cross-Section Intercomparison (GPCI) study, in which more than 20 climate and weather-prediction models participated (Teixeira et al. 2011). Thus, MAGIC with its unprecedented, intraseasonal, high-resolution ship-based observations is expected to provide constraint, validation, and support for the aforementioned modeling efforts and at the same time contribute in improving our understanding of the Sc-to-Cu transition along this GPCI transect.

From October 2012 through September 2013, the *Spirit* completed 20 round trips between Los Angeles, California, and Honolulu, Hawaii. Each trip is called a "leg," and legs are numbered sequentially as "LegxxA" for the trips from Los Angeles to Honolulu and "LegxxB" for the return trips (Fig. 1b). During the legs from Los Angeles, the *Spirit* traveled at ~21 kt (~10.5 m s^{-1}; 1 kt = 0.51 m s^{-1}) and covered the 4100-km distance in 4.5 days. The *Spirit* returned to Los Angeles at ~16 kt (~8 m s^{-1}), making the trip in approximately 6.5 days (the lower speed resulting in lower fuel costs and allowing the ship to remain on a two-week schedule; Lewis et al. 2012). The departure and arrival times of MAGIC legs are listed in appendix A. Two technicians associated with the MAGIC campaign lived on

board the *Spirit* during the deployment to maintain the instrumentation, launch radiosondes, and perform other tasks.

b. AMF2 instrumentation and data description

The AMF2 contains a state-of-the-art instrumentation suite and was designed to operate in a wide range of climate conditions and locations, including shipboard deployments. The AMF2 was located on the bridge deck of the *Spirit*, approximately 16 m above mean sea level (MSL). The primary AMF2 instruments used in the current study are 1) a Ka-band ARM zenith radar (KAZR), 2) a laser ceilometer, 3) a Vaisala weather station, 4) an inertial navigational location and attitude system (NAV), 5) the Marine Meteorological System (MARMET) installed on the mast of the *Spirit* approximately 27 m above sea level and an Infrared SST Autonomous Radiometer (ISAR), and 6) radiosondes (four or eight per day). AMF2 also contained a motion-stabilized W-band radar, a radar wind profiler, a broadband and spectral radiometer suite, aerosol instrumentation, and other instruments. The operational status of all instruments during the campaign is summarized in appendix B. There were some time periods when the KAZR was not acquiring data for various reasons (e.g., installation, power outages, etc.), but KAZR measurements were obtained for all of Leg03A through Leg08B, Leg11, and Leg14A through Leg17B. The analyses presented here are based on these data, in total 22 transits between California and Hawaii through the Sc-to-Cu transition region comprising more than 3000 h. The data are separated into two seasons: the warm season, Leg11 and Leg14 to Leg17 (25 May–6 June and 7 July–29 August 2013), and the cold season, Leg03 to Leg08 (6 October–27 December 2012).

1) KA-BAND ARM ZENITH RADAR

The KAZR, formerly known as the millimeter wavelength cloud radar (MMCR; Moran et al. 1998), is a 35-GHz profiling Doppler radar that retrieves information on the vertical distribution of the hydrometeors in the atmospheric column. Because of its short wavelength (8.6 mm), the KAZR has sufficient sensitivity to detect MBL clouds with little attenuation under moderate drizzle conditions. The KAZR might fail to detect very thin liquid clouds and it can provide inaccurate hydrometeor-layer heights during heavy precipitation because of severe radar signal attenuation (Matrosov 2007), but because a ceilometer was used [section 2b(2)] and because there was very little heavy precipitation during MAGIC, these issues should have little effect on the results of this study. The KAZR utilizes a new digital receiver that provides higher temporal (less than 2 s) and spatial (30 m) resolution than the MMCR (Widener et al. 2012). It is unaffected by Bragg scattering and has small antennas with narrow beamwidths as well as limited sidelobes (Kollias et al. 2007). During MAGIC, the KAZR was configured to have temporal resolution of about 0.4 s to oversample the ship motion, thus enabling compensation of the effects of this motion on the radar observables during data post-processing. In this study, all KAZR measurements have been averaged over 4 s, which allows for the detection of small-scale Cu.

2) CEILOMETER

A ceilometer (Vaisala model CT25K) operating at a wavelength of 910 nm was used to detect the base heights of clouds. The ceilometer's range resolution was 10 m, and its temporal resolution was near 16 s for Leg03 and Leg04 and 3 s for the other legs. To maintain the 4-s temporal resolution, it is assumed that each reported base height is representative of the entire original time period.

3) VAISALA WEATHER STATION

A Vaisala weather station WXT-520 installed as part of a suite of meteorological instruments associated with the Aerosol Observing System of the AMF2 (AOSMET) measured rain intensity at 1-s resolution, which was used to detect the presence of precipitation reaching the ground (see section 3c).

4) NAVIGATIONAL LOCATION AND ATTITUDE

NAV provided ship location and attitude with a temporal resolution of 1 s during the period between November 3 and 3 December 2012 (Leg05A to Leg07A), and 0.1 s for the rest of the deployment. As all macroscopic data are averaged over 4 s, both temporal resolutions are sufficiently accurate for the present comparisons.

5) MARINE METEOROLOGICAL MEASUREMENT AND MARINE FLUX DATASETS

The MARMETX dataset (http://www.arm.gov/campaigns/amf2012magic/) contains standard surface meteorological parameters measured by the MARMET: temperature (T), pressure (P), relative humidity (RH), and apparent and true wind speed and direction; and the sea surface skin temperature (SSST) measured by the ISAR (with an accuracy of better than 0.1°C). The Marine Flux dataset (MARFLUX; http://www.arm.gov/campaigns/amf2012magic/) contains the surface fluxes of moisture and sensible and latent heat calculated by the TOGA COARE air–sea flux algorithm (Fairall et al. 1996) using the MARMETX variables. Both MARMETX and MARFLUX have a time resolution of 1 min.

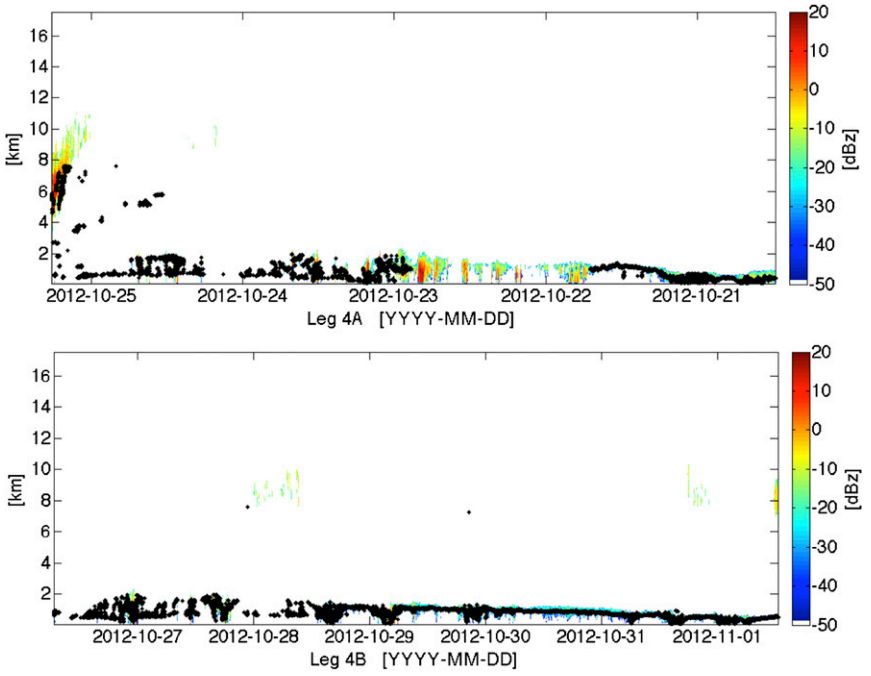

FIG. 2. KAZR reflectivity observations for (top) Leg04A and (bottom) Leg04B with the first ceilometer cloud base shown as black dots. The *Spirit* departed from California on 21 Oct 2012 and arrived in Hawaii on 25 Oct, then left on 26 Oct and returned to California on 1 Nov 2012. Graphs are shown with Los Angeles to the right and Honolulu to the left. The ceilometer data for 0000 to ~2116 UTC 22 Oct 2012 are not available.

6) ATMOSPHERIC SOUNDINGS

Standard radiosondes (Vaisala model MW-31, SN E50401) were launched every 6 h to measure vertical profiles of the thermodynamic state of the atmosphere (T, P, RH, and wind speed and direction). During Leg14, which occurred in July 2013, launches were made every 3 h to provide a more detailed picture of the atmospheric structure. Only soundings providing measurements as high as 15 km were used in this study (389 in all). The radiosondes collected data every 2 s during their ascent, providing a typical vertical resolution of 10 m in the troposphere. However, owing to the limited launching frequency (four to eight per day), sounding data can be interpolated to higher-resolution time steps with only limited confidence.

3. Methodology

a. Hydrometeor mask

A hydrometer mask was applied to the raw KAZR reflectivity measurements to identify the radar range gates that contain appreciable returns from hydrometeors. Following Rémillard et al. (2012), this mask uses the algorithm of Hildebrand and Sekhon (1974) and a two-dimensional (time–height) filter to identify the number of hydrometeor layers in the atmospheric column and their corresponding boundaries. The lowest hydrometeor boundary is not necessarily the cloud base because the KAZR cannot distinguish cloud drops from precipitation particles below the cloud base.

b. Cloud boundaries and cloud classification

To obtain cloud boundaries, the hydrometeor mask is combined with the ceilometer-generated time series of cloud-base height. The ceilometer cloud-base heights are binned to the KAZR spatial resolution, with an uncertainty of less than 15 m (the KAZR has range resolution of 30 m). Examples of the KAZR hydrometeor mask along with first ceilometer-derived cloud-base heights for Leg04A and Leg04B are shown in Fig. 2. The combination of the KAZR and the ceilometer is sufficient to characterize cloud fraction (CF) and layering in the lower troposphere (i.e., $<\sim$3 km), although hydrometeor occurrence in the upper troposphere is probably underestimated because the maximum operational range of the ceilometer is 5–6 km. However, as the analysis here pertains to MBL clouds, this underestimation should not introduce any biases.

Cloud tops for each hydrometeor layer throughout the troposphere are determined using the KAZR-derived hydrometeor mask. In liquid clouds, KAZR

TABLE 1. Cloud types and characteristics used to differentiate them in the identification algorithm (''Ind'' stands for indeterminate).

		Type					
				MBL			Cu congestus and deep convective
		High level	Midlevel	Sc	Cu	Ind	
Minimum cloud base		≥6 km	3–6 km	<3 km*	<3 km*	<3 km*	<3 km
Maximum cloud top		—	—	<3 km	<3 km	<3 km	≥3 km
Duration		—	—	≥20 min	<20 min	≥20 min	—
Cloud-top height standard deviation	20 min to 2 h	—	—	<100 m	—	≥100 m	—
	2 to 10 h	—	—	<160 m	—	≥160 m	—
	>10 h	—	—	<200 m	—	≥200 m	—

* Minimum cloud base for MBL clouds is either below 3 km or undetermined.

reflectivity measurements below the first cloud-base height determined by the ceilometer are used to characterize precipitation (see next section). If no ceilometer data are available, no KAZR data below 300 m are used, since they often contain artifacts (especially when no precipitation is present). In cases when the first ceilometer-derived base height is 100 m or more less than the first KAZR-defined hydrometeor base height, the two clouds are considered independent, with the first cloud-top height undetermined; otherwise the first KAZR hydrometeor top is considered to be the first cloud top.

Once the cloud boundaries are determined, each time–height cluster of KAZR echoes with more than 25 connected pixels (in time–height space) is considered to be a cloud entity. To obtain realistic bases of multiple-layer cloud entities, the bases of the second cloud level are further smoothed according to the ceilometer-derived base heights. KAZR echoes below the newly defined cloud bases are neglected. Each cloud entity is categorized into one of four types based on its average base and top heights (Table 1; see Fig. 3a as an example): high-level, midlevel, MBL, or cumulus congestus and deep convective. High-level clouds have average base heights of at least 6 km. Midlevel clouds have average base heights between 3 and 6 km. MBL clouds have average base heights and top heights less than 3 km, or have undetermined average top heights. Cumulus congestus and deep convective clouds have average base heights less than 3 km but average top heights of at least 3 km. The statistical results of cloud properties presented in this study are not sensitive to the specific values chosen for the thresholds.

An MBL cloud layer is detected if more than 10% of cloud bases are measured over a continuous range of heights during 1 h (a one-gate gap is allowed). The cloud bases here refer to the first and second ceilometer-derived bases and the first three hydrometeor-mask bases.

As the focus of this study is MBL clouds, emphasis is placed on these clouds, which are further divided into three subtypes: stratocumulus, cumulus, and indeterminate (e.g., Figs. 3b and 3c). Sc are low clouds composed of an ensemble of individual convective elements that together assume a layered form (Wood 2012), whereas Cu clouds are separate convective elements. The difference between Sc and Cu in this study is based on their time durations: a cloud is defined as Sc if it lasts more than 20 min, and as Cu if its duration is less than 20 min. Sc clouds are also required to have a narrow cloud-top height distribution that is restricted by a specific standard deviation threshold that depends on its duration (see Table 1 for details). The remaining MBL cloud clusters make up the subtype ''indeterminate.'' Because of the limited nature of the MAGIC observations (1D in distance/time and height), these cloud types are not mutually exclusive.

Because of their ship-based origin, the cloud macroscopic data for each leg depend on both time and location (e.g., Figs. 1 and 2). To account for slight ship-course deviations between different legs (Fig. 1b), all of the cloud macroscopic data are binned to a uniform great-circle route with 40-m resolution (the approximate distance covered by the ship in 4 s) in order to examine the evolution of cloud properties along this representative great-circle transect. Finally, all the cloud macroscopic data are averaged over 36 km (the approximate distance covered by the ship in 1 h) and converted to the corresponding latitude along the great-circle route. The frequency of occurrence of MBL cloud every 36 km are considered to represent the CF over that area and are referred to as CF_{36} in this paper.

c. *Precipitation classification*

KAZR observations, the KAZR-derived hydrometer mask, ceilometer-derived cloud-base heights, surface rainfall occurrence from the weather stations, and 0°C isotherm heights derived from interpolated radiosonde data are used characterize precipitation. KAZR echoes are classified as either cloud or precipitation; no attempt is made to distinguish ice hydrometeors from liquid cloud drops or precipitation. Because the cloud-base

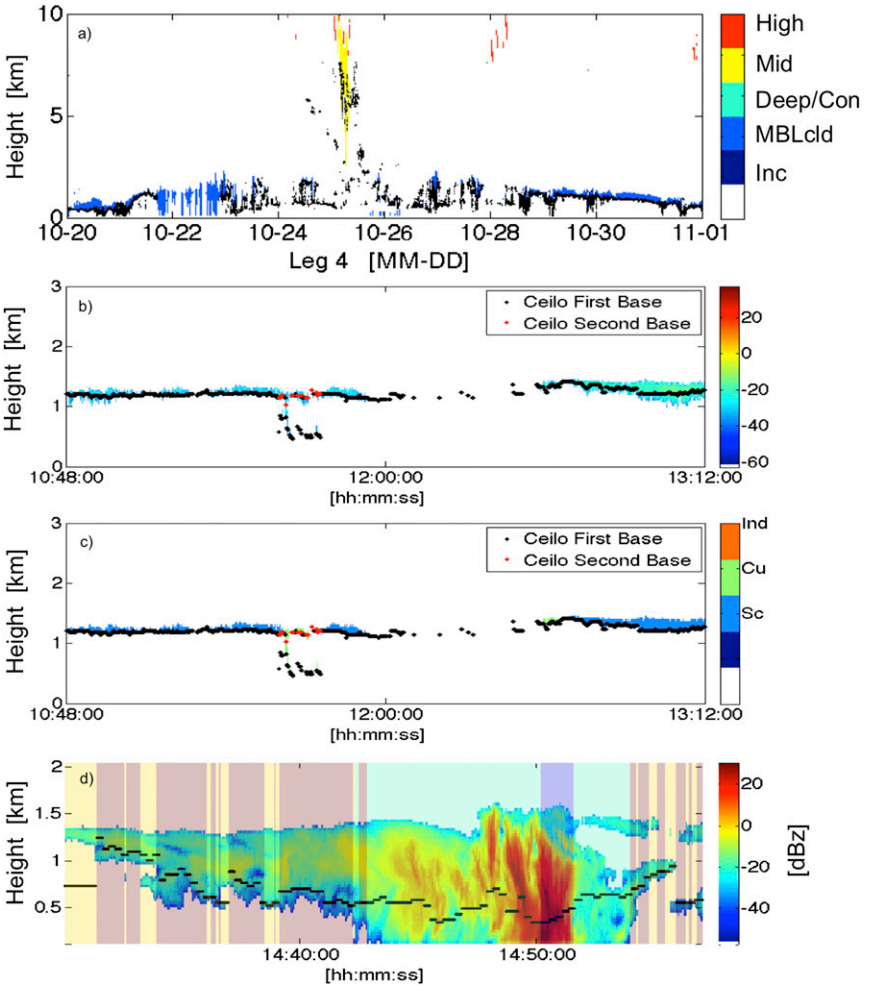

FIG. 3. (a) Cloud classifications for Leg04 with the first ceilometer cloud base shown as black dots. The corresponding KAZR reflectivities can be seen in Fig. 2. (b) KAZR reflectivities with the first and second ceilometer cloud base shown as black and red dots respectively for a short time segment on 21 Oct 2012 during Leg04A. (c) MBL cloud classifications with the first and second ceilometer cloud base shown as black and red dots for the same time period as that shown in Fig. 3b during Leg04A. (d) KAZR reflectivities with the first ceilometer cloud base shown as black dots for a short time period on 28 Oct 2012 during Leg04B. The pink, light blue, and purple backgrounds indicate the occurrence of virga, MBL drizzle, and heavy MBL drizzle, respectively; the yellow background indicates no precipitation during that time period.

heights are determined from the ceilometer data, every KAZR echo below the first cloud-base height is classified as precipitation. The ceilometer quality control flag was checked to ensure that no water was present on the ceilometer window (which would occur in the case of intense precipitation reaching the surface), since this would strongly attenuate the signal and result in inaccurate readings.

Precipitation is classified into five types (Table 2): virga, drizzle, warm rain, cold rain, and deep convective rain (e.g., Fig. 3d). Precipitation that is not detected at the surface is either virga or drizzle. The distinction between the two is based on the detection of KAZR echoes in the lowest range gate (around 120 m ASL before Leg11A, and 240 m ASL for the later legs): virga is defined as precipitation that is detected at least 50 m below the ceilometer cloud base and does not reach the lowest KAZR range gate, whereas drizzle is detected at the KAZR lowest range gate. This distinction provides a qualitative indicator of light rain intensity and indicates the portion of the subcloud layer affected by evaporation. Under this proposed definition only rain that falls through a cloud and not that from the side of a cloud could be considered virga. Precipitation is defined as warm (cold) rain when it is detected at the surface and when the first KAZR-derived cloud top is above 3 km but

TABLE 2. List of liquid precipitation types and their main characteristics used to differentiate them.

	Type				
	Virga	Drizzle	Warm rain	Cold rain	Convective rain
Echo base	> First gate	= First gate	= First gate	= First gate	= First gate
Base reflectivity	—	<0 dBZ	>0 dBZ	>0 dBZ	>0 dBZ and >first top reflectivity
Surface rain	No	No	Yes	Yes	Yes
First cloud-top height	Below 0°C isotherm	Below 0°C isotherm	Below 0°C isotherm	Above 0°C isotherm	—
Echo below cloud base	Yes (50 m lower)	Yes (50 m lower)	Possible	Possible	Possible

lower (higher) than the 0°C isotherm height, regardless of the ceilometer-derived cloud-base height. Precipitation is defined as convective rain when it is detected at the surface and when the radar reflectivity at the lowest range gate is greater than 0 dBZ and also greater than that at the first KAZR cloud-top height. Similar to the cloud macroscopic data, the precipitation data for each leg are averaged over 36 km along the great-circle route.

d. Radiosonde analysis

Radiosonde data are used to determine the thermodynamic structure of the lower atmosphere. Emphasis in this study is placed on identifying the inversion and transition layers, which are closely associated with MBL stratification and MBL clouds. The inversion layer is defined as all levels around the maximum increase of temperature with height that occurs between 500 m and 3 km that have an increase of temperature and a decrease in water vapor mixing ratio (r) with height [see Rémillard et al. (2012) for more details].

Following the algorithm of Yin and Albrecht (2000), a parameter μ is defined for each level below the inversion base in terms of the potential temperature (θ) and r:

$$\mu = -\left(\frac{\partial\theta}{\partial P} - \frac{0.608\theta}{1+0.608r}\frac{\partial r}{\partial P}\right), \tag{1}$$

and the transition layer is defined whenever the maximum value of μ is positive and consists of all levels below the base of the inversion at which μ is greater than 1.3 times its mean value over the entire region below the inversion. Examples of the sounding-derived inversion and transition layers under conditions of broken Cu and overcast Sc are illustrated in Figs. 4a and 4b, respectively.

The sounding data for each vertical profile are smoothed prior to any analysis using only the next-nearest points to remove small-scale variability and to provide smooth local gradients. To preserve the features of the transition and inversion layers, a layer-by-layer averaging procedure is performed when averaging various profiles together (Augstein et al. 1974; Yin and Albrecht 2000; Rémillard et al. 2012). Between the surface and 3 km, the profiles are broken into five layers: the layer below the transition, the transition layer, the layer between the transition and the inversion, the inversion layer, and the layer above the inversion. Each layer is averaged separately using a normalized height coordinate (from 0 to 1) and is combined with other layers using the averaged base and top heights of the layers as the height coordinate.

The difference between equivalent potential temperature at the inversion top $\theta_{e(\text{inv\_top})}$ and base $\theta_{e(\text{inv\_base})}$,

$$\Delta\theta_e = \theta_{e(\text{inv\_top})} - \theta_{e(\text{inv\_base})}, \tag{2}$$

provides information on the stability of the MBL: lower values of $\Delta\theta_e$ indicates greater cloud-top entrainment instability because the entrained air, after becoming saturated, would be more negatively buoyant and would continue to sink (Lilly 1968; Deardorff 1980). Additionally, numerical calculations demonstrate that the entrainment rate increases abruptly when $\Delta\theta_e$ decreases below a critical value (Deardorff 1980). Approximately 10% of the profiles contained an artificial peak in water vapor mixing ratio immediately above Sc due to the wet-bulb effect of the radiosondes; when this occurred, $\theta_{e(\text{inv\_top})}$ was replaced by the value of θ_e immediately below this peak.

The inversion strength is quantified using the lower-tropospheric stability (LTS; Klein and Hartmann 1993) and by the estimated inversion strength (EIS; Wood and Bretherton 2006). LTS is defined as the difference between the potential temperature at 700 hPa (θ_{700}) and that at the surface (θ_{surface}),

$$\text{LTS} = \theta_{700} - \theta_{\text{surface}}. \tag{3}$$

EIS is defined as

$$\text{EIS} = \text{LTS} - \Gamma_m^{850}(Z_{700} - \text{LCL}), \tag{4}$$

where Γ_m^{850} is the moist adiabat at 850 hPa, Z_{700} is the 700-hPa height, and LCL is the lifting condensation level. The LCL can be approximated by Epsy's formula (Bohren and Albrecht 1998) in terms of the surface

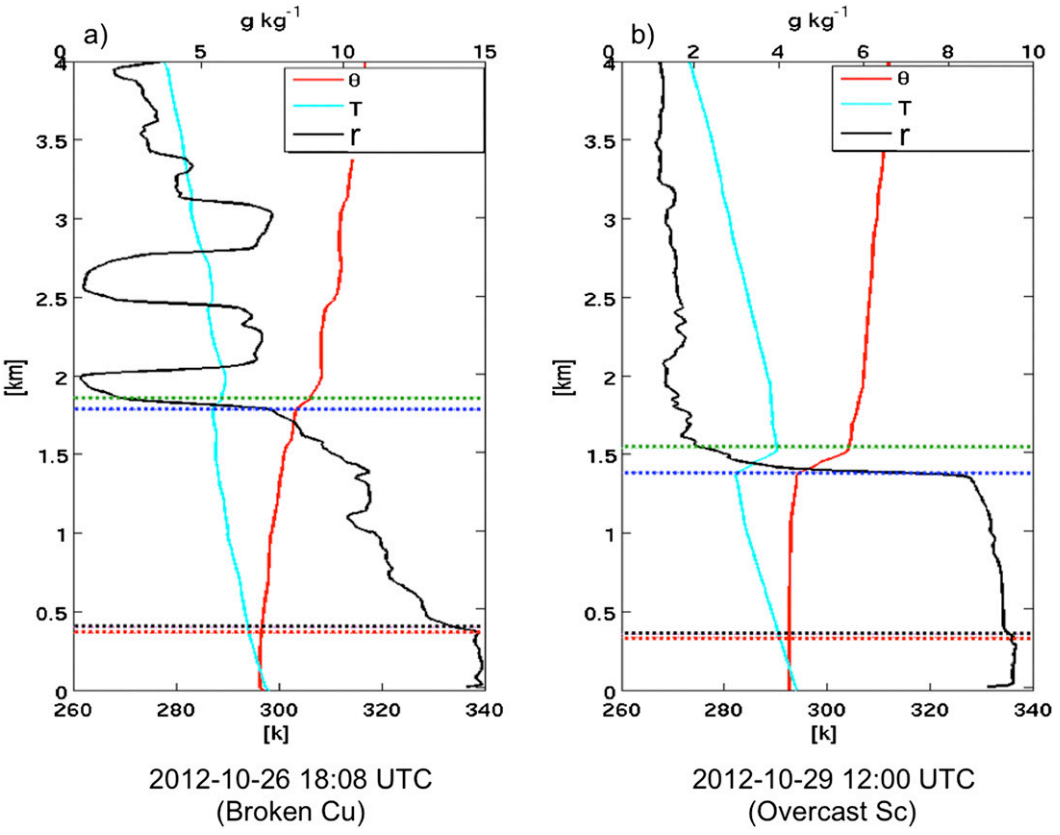

FIG. 4. Profiles of temperature (T), potential temperature (θ), and mixing ratio (r) from soundings. Green and blue dashed lines show the inversion tops and bases, while black and red dashed lines show the transition tops and bases. (a) Sounding launched at 1808 UTC 26 Oct 2012, with broken Cu overhead. (b) Sounding launched at 1200 UTC 29 Oct 2012, with overcast Sc overhead.

values of the air temperature (T_s), dewpoint temperature (T_d), dry adiabatic lapse rate (Γ_d), and pseudoadiabatic lapse rate (Γ_s) as

$$\mathrm{LCL} = \frac{T_s - T_d}{\Gamma_d - \Gamma_s}; \tag{5}$$

numerically, the value of LCL (in m) is approximately 125 times the difference $T_s - T_d$ (in K). EIS, and previously LTS, have been shown to correlate well with the occurrence of the Sc-to-Cu transition (Wyant et al. 1997); however, EIS is a more physically based quantity as it accounts for the influence of the accumulated static stability between the inversion and the 700-hPa level (Wood and Bretherton 2006).

To derive the statistics, all the sounding data are averaged over 36 km and converted to corresponding latitude along the great-circle route. As the statistics of the inversion layer presented below are based primarily on measurements from radiosondes, which were launched four (eight) times every day (see section 2b), each sounding profile is assumed to be representative of the atmospheric structure over the 6 h (3 h) time around the sounding. Because of the sparseness of these data, these statistics might not be as robust as those derived from the radar, but nonetheless they are expected to accurately represent the observed trends.

e. *Systematic MBL decoupling and Sc breakup detection*

The commencement of the systematic MBL decoupling (DE) and Sc breakup (CB) toward Hawaii has been determined for each leg in order to better understand their triggering factors. At each location, the difference in the mean water vapor specific humidity (q_v) between the bottom 25% of the MBL and the top 25% of the MBL is calculated:

$$\Delta q = q_v(\mathrm{bot}) - q_v(\mathrm{top}). \tag{6}$$

This quantity is related to Δz_b, the difference in the Sc cloud bases formed below the inversion (z_b) and the LCL:

$$\Delta z_b = z_b - \mathrm{LCL}, \tag{7}$$

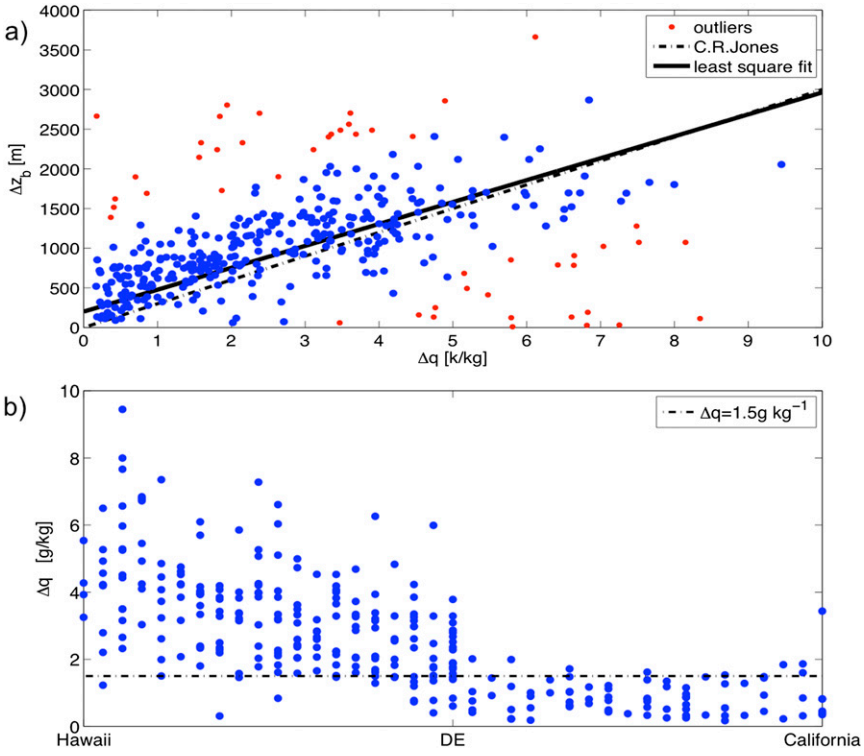

FIG. 5. (a) The scatterplot of radiosonde-derived Δq for all the legs and maximum Δz_b within four degrees longitude surrounding each radiosonde. The solid black line is the least squares fit with slope 276 m kg g^{-1} and intercept 200 m. The dashed black line represents the thermodynamic argument derived in Jones et al. (2011). The red dots indicate outliers outside 1.5 standard deviations of the least squares fit. (b) Radiosonde-derived Δq for all the legs along the normalized path from California to DE to Hawaii.

where z_b is calculated as the maximum MBL cloud bases (averaged over 36 km) within four degrees longitude surrounding each radiosonde. The linear relationship between Δq and Δz_b (Fig. 5a) with the slope (276 m kg g^{-1}) and intercept (200 m) comparable to those found in Jones et al. (2011), demonstrate that Δq is a robust proxy for Δz_b. Some scatter is introduced since Δq comes from a single profile while Δz_b is an averaged maximum value. Biases might be introduced when no Sc was detected near a radiosonde or when MBLH was not well represented due to the very shallow MBL near the coast of California. Thus only those radiosondes within 1.5 standard deviations of the least squares fit and that to the west of 123°W were used (336 in total). A threshold of $\Delta q > 1.5\,\mathrm{g\,kg^{-1}}$ (or equivalently $\Delta z_i > 600$ m) is found appropriate to capture the systematic decoupled MBL (Fig. 5b). Compared to the threshold of $\Delta q > 0.5\,\mathrm{g\,kg^{-1}}$ ($\Delta z_i > 150$ m) for all kinds of decoupling in VOCAL-REx (Jones et al. 2011), the systematic decoupling showed much stronger moisture stratification below the inversion. Subsequently, the DE during each transect is then defined as the most easterly profile of a group of profiles with continuous decoupling features ($\Delta q > 1.5\,\mathrm{g\,kg^{-1}}$). Between the detected and the nearest east radiosonde launches, the Δq criteria for decoupling is replaced by the difference of the instantaneous ceilometer-derived cloud base height and LCL calculated by the ship-measured T and RH. Compared to the systematic decoupling, the weak decoupled MBL is also studied in this paper and is defined as the MBL with $\Delta z_i >$ 150 m [consistent with Jones et al. (2011)].

Because of mesoscale influences, CF_{36} sometimes shows variability and does not represent well the major cloud evolution along the transect. To reduce the effects of mesoscale variability and to more objectively capture CB, the frequency of occurrence of the MBL clouds was averaged over 108 km (CF_{108}). CB is then defined as the location along the transect from California to Hawaii where CF_{108} decreased from being greater than 80% for at least three continuous points (324 km) east of 130°W to being less than 15%. Values of CF_{108} were generally not sensitive to the above criteria. No cloud breakup points are determined if values of CF_{108} east of 130°W were not sufficiently high (Leg06A, Leg06B, Leg08A, Leg08B, and Leg17B) or if they did not become sufficiently low (Leg15B). Those legs

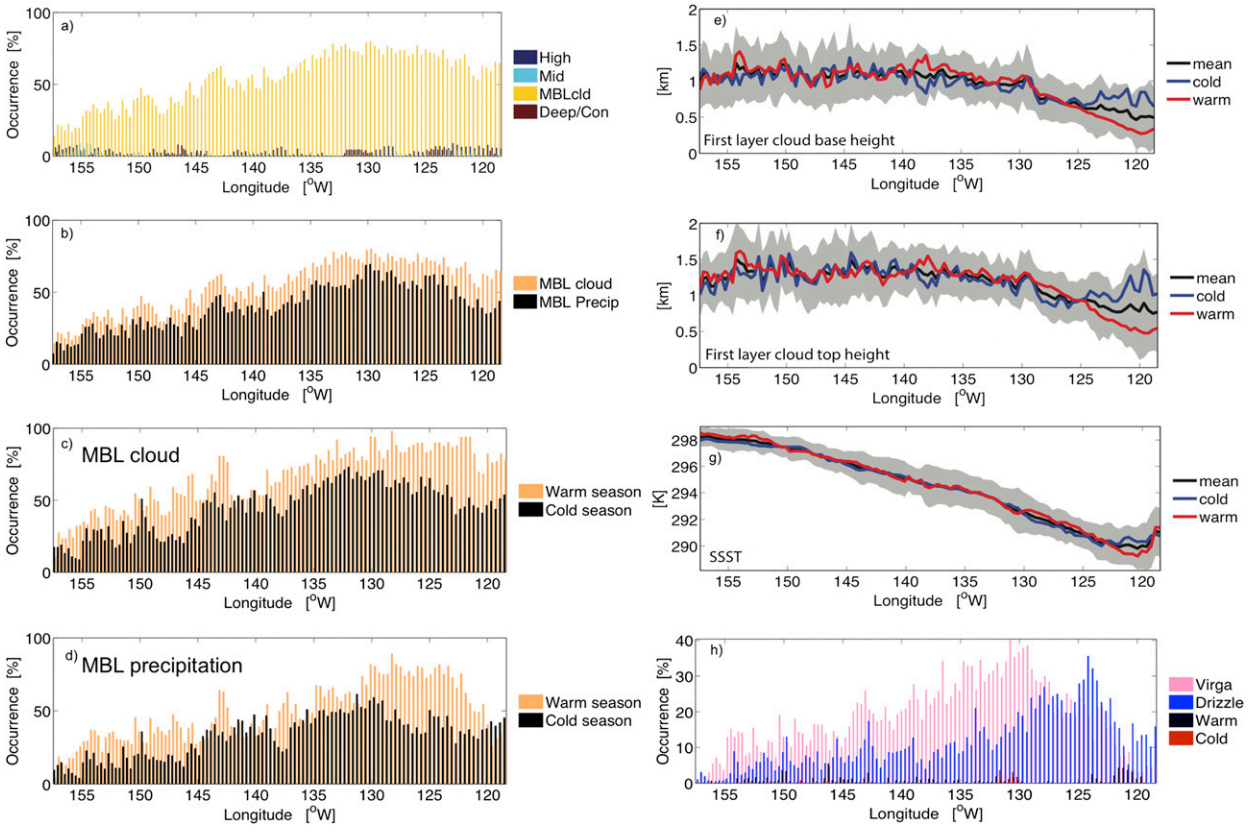

FIG. 6. Frequencies of occurrence along the MAGIC transect of (a) the four main cloud types, (b) MBL clouds and observed MBL-cloud liquid precipitation; (c) MBL clouds and (d) observed MBL-cloud liquid precipitation during the warm and cold season during the warm season (Leg11, Leg14–Leg17: 25 May–6 Jun 2013, 7 Jul–29 Aug 2013) and during the cold season (Leg03–Leg08: 6 Oct–27 Dec 2012). Also shown are the total and seasonal mean along the MAGIC transect of (e) first cloud-base heights, (f) first cloud-top heights, and (g) SSST. The black line shows the total mean; the blue and red lines show the mean for the cold and warm season, respectively. The gray shaded region indicates one standard deviation of the mean. (h) Frequencies of occurrence along the MAGIC transect of liquid precipitation types.

are associated with either midlatitude or tropical cyclones, or very strong cloud outbreaks thus do not represent the Sc breakup in a general sense, and their exclusion helps to elucidate the more general aspects of the transition.

4. Results

The results presented below are separated into two sections. The first section includes general statistical description of MBL clouds, precipitation, thermodynamics, and their seasonal behavior. The second section focuses on the study of MBL systematic decoupling and cloud breakup.

a. General statistics of MBL clouds, precipitation, and thermodynamics

1) CLOUD AND PRECIPITATION OCCURRENCE

The fraction of time that the four main cloud types defined in section 3b are detected (i.e., their frequencies of occurrence over individual legs) is shown in Fig. 6a. MBL clouds are by far the most frequently observed cloud type, and all other types contribute less than 10% to the total observed hydrometeor occurrence in the column. The frequency of occurrence of MBL clouds has a broad maximum near 75% between 125° and 135°W and decreases steadily to values near 20% near Hawaii. Lower values of MBL cloud occurrence are also observed near the coast of California. The frequency of occurrence of precipitation from MBL clouds (Fig. 6b) exhibits a very similar pattern to that of MBL cloud occurrence.

A seasonal breakdown of MBL cloud occurrence is shown in Fig. 6c. The frequencies of occurrence of MBL clouds in the warm season and the cold season exhibit generally similar spatial patterns. During the warm season a broad maximum near 90% between ~122° and ~132°W is observed, whereas that during the cold season a maximum near 70% between ~128° and

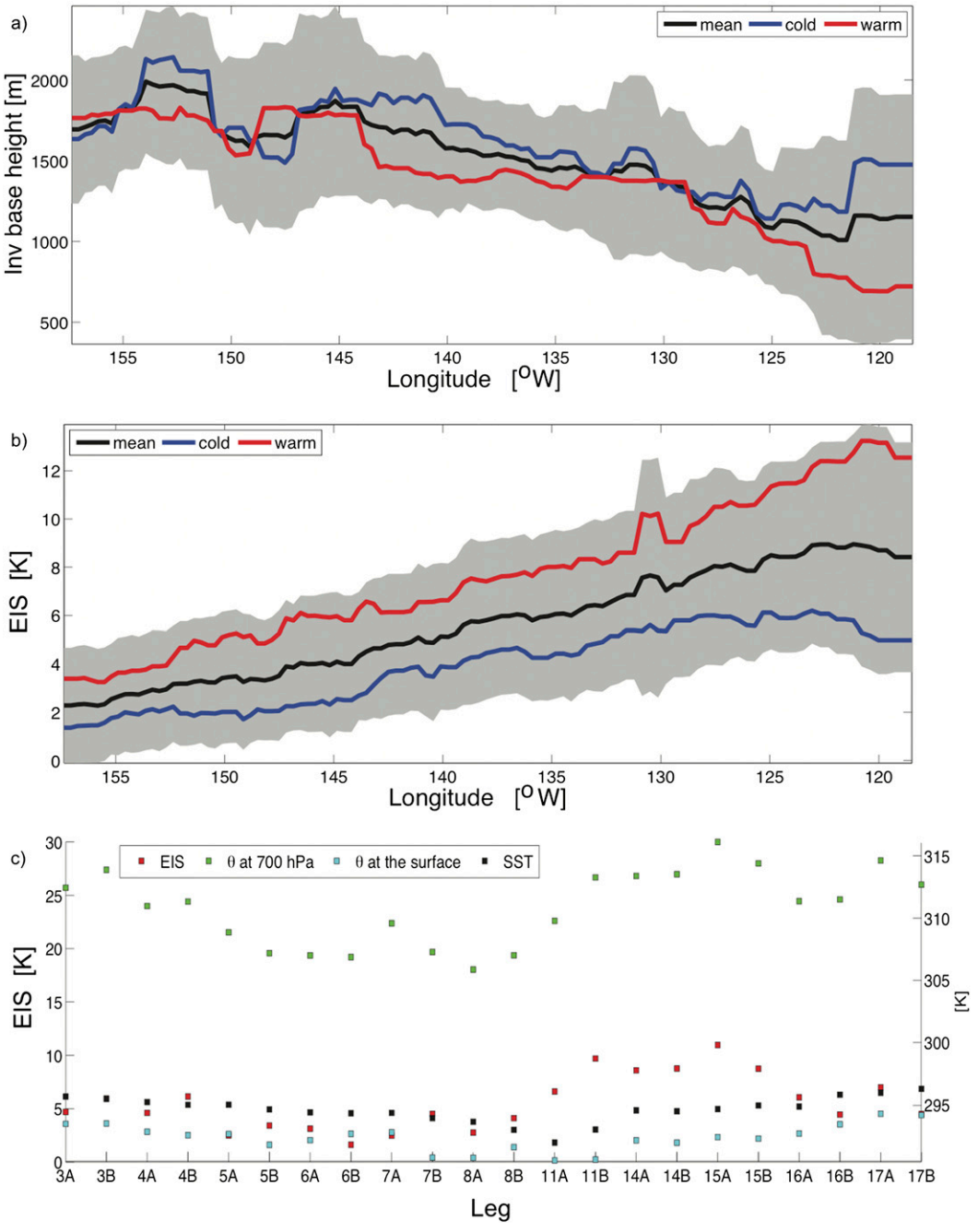

FIG. 7. Total and seasonal mean of (a) MBLH and (b) EIS along the MAGIC transect. The gray shaded region indicates one standard deviation of total. The black line shows the total mean, the blue line shows the mean of the cold season, and the red line the mean for the warm season. (c) Leg-mean values of EIS, SSST, potential temperature at 700 hPa, and potential temperature at the surface.

~132°W is observed. On average, the observed MBL cloud occurrence in the warm season is 20%–40% higher than that observed in the cold season.

As expected, the frequency of occurrence of precipitation (Fig. 6d) is also generally higher during the warm season than during the cold season. During the warm season precipitation exhibits a maximum of ~80% between ~123° and ~131°W, but during the cold season the broad maximum of ~55% is observed between ~128° and ~136°W. In contrast to the relatively high frequency of occurrence of clouds during the warm season east of 124°W, the corresponding frequency of

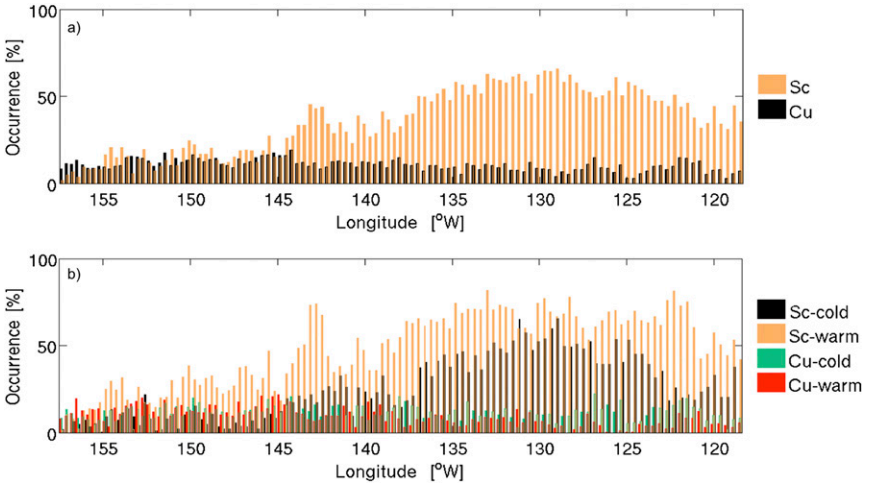

FIG. 8. Frequencies of occurrence of cloud types (a) over the entire deployment and (b) during the cold season and warm season.

occurrence of precipitation decreases rapidly. This might be attributed to the presence of thin clouds at this region (average thickness of 180 m east of 124°W compared to 300 m west of 124°W).

The mean cloud-base height (H_b; Fig. 6e) and mean cloud-top height (H_t; Fig. 6f) of the lowest cloud layer show little seasonal variability except for the regions east of 125°W. Mean values of H_b increase gradually from 0.6 km near the coast of California to 1 km near 135°W and remain at around 1 km farther west but exhibit increasing fluctuations, reflecting the intermittent presence of small-scale Cu clouds below the Sc. The H_t values are on average 230 m greater than those of H_b and also exhibit fluctuations west of 135°W. East of 125°W we found the most noticeable difference in H_b and H_t between the warm and cloud season. The lower H_b east of 125°W during the warm season might be attributed to the stronger coastal upwelling that results in lower SST (Fig. 6g), while the higher H_t east of 125°W during the cold season might be attributed to a frontal system that occurred during Leg06B and a low pressure system during Leg07B.

Most of the precipitation produced by MBL clouds is in the form of virga (Fig. 6h). Virga is the dominant precipitation type over the entire transect except for the region east of 126°W. The virga frequency of occurrence peaks at 40% near 130°W, whereas that of drizzle (precipitation that reaches the lowest range gate) exhibits a sharp maximum of more than 30% near 124°W, contributing to the noticeable peak of precipitation frequency at this location (Figs. 6b,d). The increasing frequency of occurrence virga and decreasing frequency of occurrence of drizzle from 124° to 130°W (Fig. 6h) might be attributed to the increasing cloud-base height (Fig. 6e) caused by the warmer SST (Fig. 6g) away from the California coast. The low frequencies of occurrence (less than 10%) of both virga and drizzle near Hawaii are consistent with the low frequency of occurrence of MBL clouds there (Figs. 6a–c). At the same time, the low frequencies of occurrence of both virga and drizzle east of 124°W is associated with the presence of thinner clouds in that region (Figs. 6e,f) and to the higher in-cloud cloud droplet concentrations. The mean surface CCN at 119°N is on average 150 cm^3 higher than that around 122°W (Lohmann and Feichter 2005).

2) SPATIAL AND SEASONAL BEHAVIOR OF MBLH AND EIS

The mean and seasonal values of MBLH and EIS [Eq. (4)] along the MAGIC transect are shown in Fig. 7. The mean MBLH (Fig. 7a) generally increases from California to Hawaii, with slightly lower values in the warm season. The largest differences in MBLHs between the warm season and cold season are observed east of 125°W, with those observed during the cold season being nearly twice as high as those during the warm season near the coast of California. The low MBLH east of 125°W during the warm season results in thin clouds [see section 4a(1)] and correspondingly a low frequency of precipitation there (Fig. 6d). The deeper MBL during the cold season is consistent with the high H_t (Fig. 6f), which might be due to synoptic influences [see section 4a(1)]. The decrease in MBLH between 145° and 150°W can also be attributed to synoptic influences and is discussed below. The trend in MBLH along the MAGIC transect (Fig. 7a) follows that of H_t (Fig. 6f) east of 135°W, indicating the capped feature of the MBL, while values of H_t west of 135°W are generally less than those of MBLH, indicating MBL decoupling and Cu-under-Sc cloud regimes.

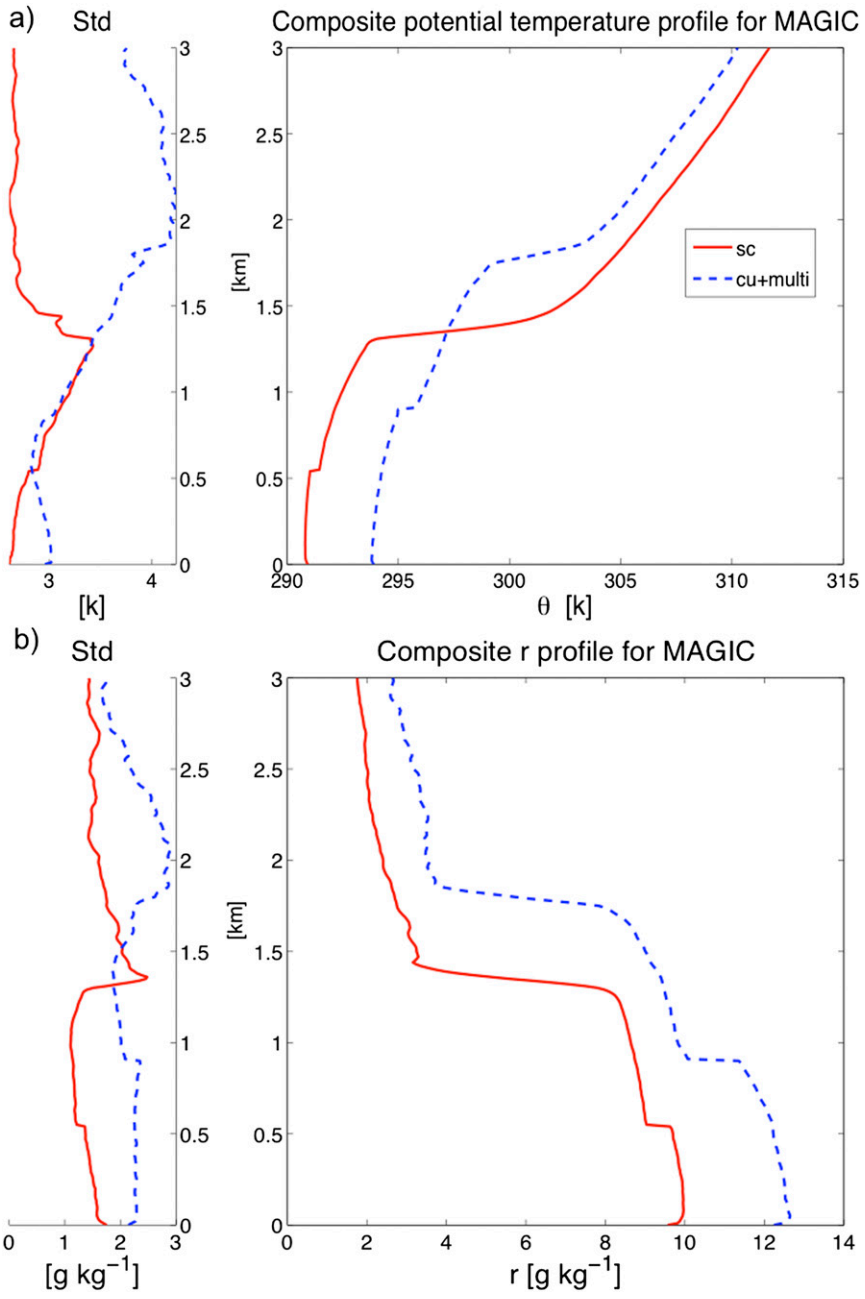

FIG. 9. Profiles of means and standard deviations of (a) potential temperature and (b) water vapor mixing ratio composed over the cases with single stratocumulus at the inversion level (blue dotted line), and single cumulus at the transition level together with multiple MBL clouds (red solid line), both of which must contain a transition layer.

The mean EIS (Fig. 7b) decreases gradually from 9 K near the coast of California to around 2 K near Hawaii, with values in the warm season being 1–3 K higher and those during the cold season 1–3 K lower, the differences decreasing toward Hawaii. EIS shows a strong linear relationship with SST along the transect (figure not shown), while in terms of the seasonal variability, leg-mean EIS is mainly determined by the leg-mean potential temperature at 700 hPa (Fig. 7c). This quantity exhibits a larger seasonal variability, ranging from 7 to 11 K among different legs due to the subsidence of the dry warm air from above the inversion layer, while θ_{surface}, which depends largely on SST, varies less than 1 K between seasons.

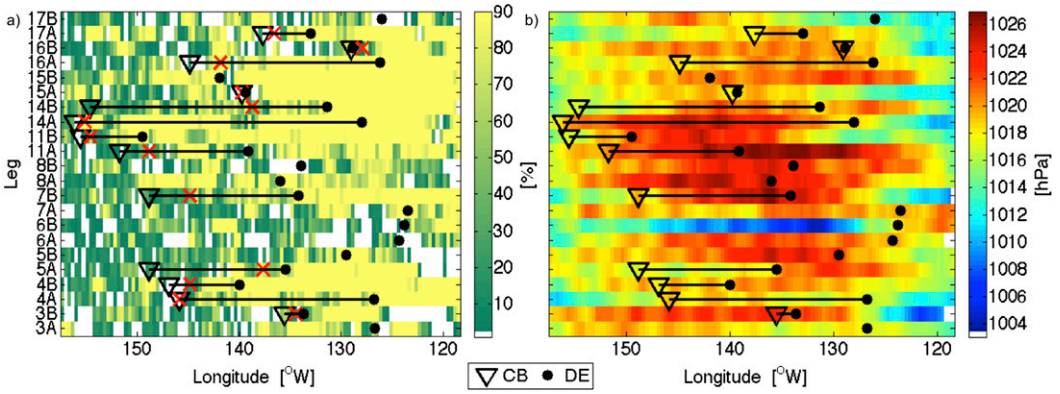

FIG. 10. (a) CF_{36} and (b) the sea surface pressure along the MAGIC transect for individual legs. The black triangle and the black dots indicate the cloud breakup points (CB) and the starting points of the MBL systematic decoupling (DE). The red crosses in (a) indicate the location when CF_{108} drops to below 50% before CB. White spaces in (a) denote times when CF_{36} was less than 10%, and those in (b) denote missing data.

It is likely that the seasonal variability of EIS (Fig. 7b) contributes to the seasonal variability in the frequency of occurrence of MBL clouds (higher amount of MBL cloud in the warm season and lower in the cold season), consistent with the conclusion of Wood and Bretherton (2006) that stratus cloud fraction is largely determined by EIS. The higher frequency of occurrence of MBL clouds during the warm season when EIS was higher (Fig. 6c) reflects the importance of the strong warm-season large-scale Hadley cell (Xu and Cheng 2013) that brings dry warm air downward, leading to higher values of θ_{700} (Fig. 7c).

3) Sc and Cu occurrence and thermodynamic features

Frequencies of occurrence of the two important MBL cloud types, Sc and Cu, are examined in this section. Statistics of total and seasonal occurrence of Sc and Cu are shown in Fig. 8. The frequency of occurrence of Sc attains a broad maximum near 60% between 125° and 135°W, and decreases to near 0% near Hawaii. The decrease in frequency of occurrence of Sc is not uniform along the MAGIC transect, and is greatest near 137°W and near 144°W, consistent with the sharp decreases in MBL cloud occurrence (Fig. 6a) at these locations. In contrast, the frequency of occurrence of Cu is always low, but steadily increases from near 5% near the coast of California to over 10% near Hawaii. Sc are more frequently observed during the warm season than during the cold season, while the occurrence of Cu is almost the same for both seasons, with slightly more frequent cold-season Cu close to the coast of California and slightly more warm-season Cu close to Hawaii.

The comparison between ceilometer-detected Sc base height and MBLH from 143 corresponding radiosondes indicate that 80% of the Sc clouds formed directly below the MBL inversion. Accordingly ceilometer-detected Cu bases heights show broader distribution but mainly occur near the top of the transition layer detected in 74 corresponding radiosondes (figures not shown). Figure 9 shows the averaged thermodynamic structure for Cu (including multilayer MBL cloud) and single-layer Sc. A total of 141 radiosondes were analyzed: 104 with Sc near the inversion (Sc top no more than 200 m below the MBLH) and 37 with Cu near the transition or multilayer cases (Cu base more than 200 m above the transition-layer tops). Application of a layer-by-layer averaging method for the soundings for each cloud category (see section 3d for details) requires detectable inversion and transition layers. Analyses of the MAGIC sounding data indicate that both layers are present in the vast majority (94%) of the soundings. Note that the presence of a transition layer does not necessarily indicate a systematic decoupled MBL (see section 3e).

As seen in Fig. 9, the large vertical gradients in potential temperature and water vapor mixing ratio near 1.5 km indicate the heights and strengths of the inversion layers, while the smaller changes below 1 km correspond to transition layers (Fig. 9). The standard deviations of both potential temperature and mixing ratio for both categories are relatively small below the inversion layer, indicating little seasonal variability in profiles of these quantities. Sc cases exhibit lower inversion- and transition-layer heights than Cu cases, and they have greater potential temperature differences across the inversion (around 10 K compared to near 5 K for Cu); the mixing ratio differences across the inversion are nearly the same for both cases, around $6\,g\,kg^{-1}$. Sc cases exhibit smaller jumps across the transition layer than Cu for both potential temperature (<0.5 K compared to near 1 K for

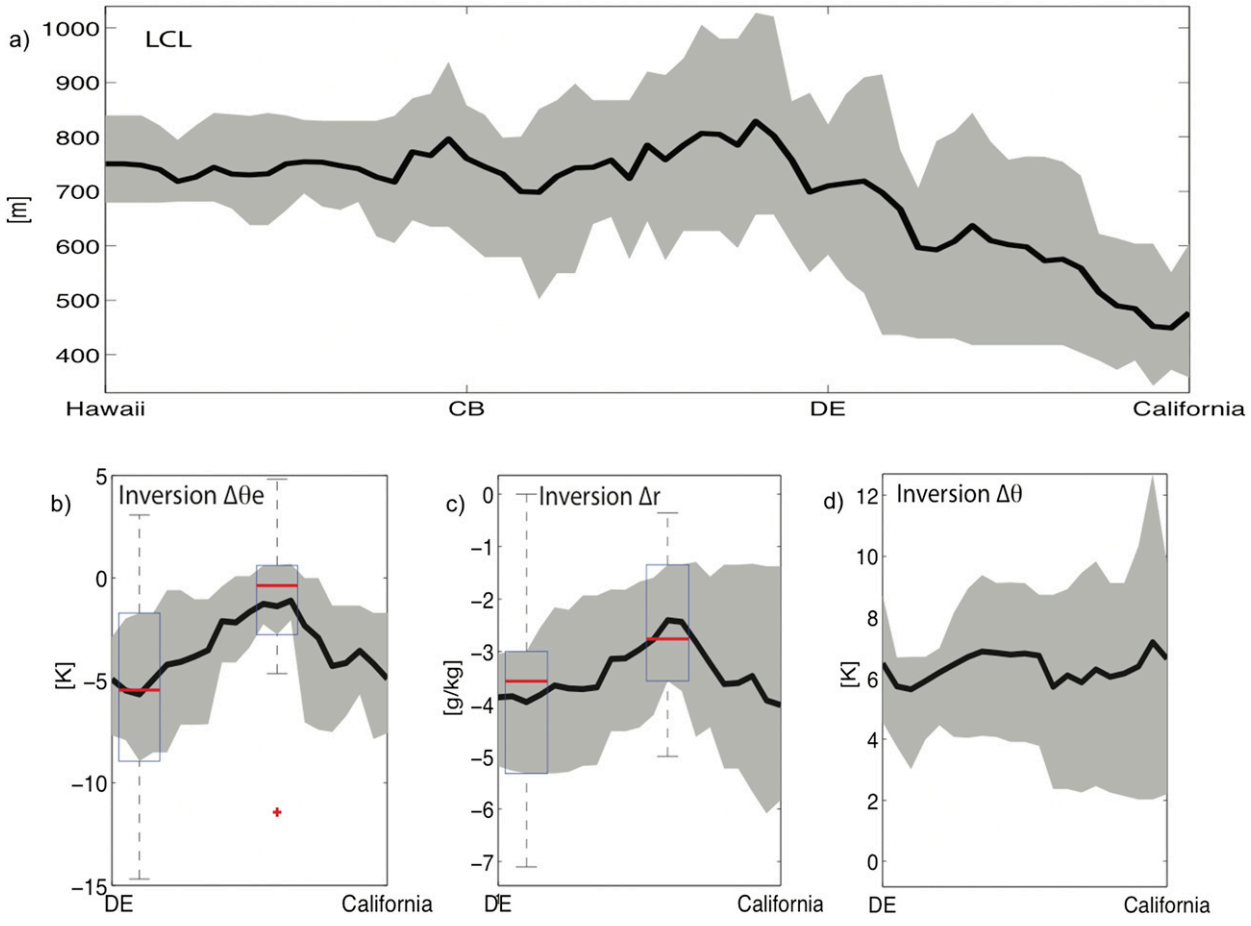

FIG. 11. Total mean of (a) the radiosonde-derived LCL along the normalized path from California to Hawaii, (b) the equivalent potential temperature difference across the inversion, (c) the mixing ratio difference at the inversion, and (d) the potential temperature difference at the inversion along the normalized path from California to DE. Gray shaded region indicates interquartile range. The boxplot in (b) and (c) indicates the location of the maximum and minimum value near DE, the difference between the two is significant at 95% confident level.

Cu) and mixing ratio ($<1\,g\,kg^{-1}$ compared to $2\,g\,kg^{-1}$ for Cu); thus Cu cases are associated with a much stronger transition layer than Sc, implying a greater chance of a decoupled MBL. However, this stronger transition results in part because the cumuli help maintain the transition layer by mixing dry and warm air from the free troposphere downward.

b. *MBL systematic decoupling and cloud breakup*

The locations of DE and CB for each leg are shown in Fig. 10. Consistent with previous studies (e.g., Albrecht et al. 1995a; Bretherton and Pincus 1995; Wyant et al. 1997; Sandu and Stevens 2011), DE occurred east of CB (when the latter was determined) on all legs. In this section, legs with both DE and CB detected are further examined with the intention of discussing some of the potential controlling factors that are usually neglected in the numerical simulations.

1) POSSIBLE CONTROLLING FACTORS OF MBL SYSTEMATIC DECOUPLING

Since DEs and CBs occurred at different locations for individual transects, a normalization of each leg is required in order to develop composites of variables across these points. Each leg is divided into three regions: east of DE, between DE and CB, and west of CB, and the distance along the transect in each region is normalized (i.e., for each leg, the distance from California to any location east of DE is divided by the distance between California and CB, and similarly for the region between DE and CB, and CB and Hawaii).

The radiosonde-derived LCL, shown in Fig. 11a as a function of this normalized distance, increases from 450 to 750 m east of DE, decreases slightly to the west of DE and remains at around 750 m to the west of CB. Numerical simulations accurately capture the increasing

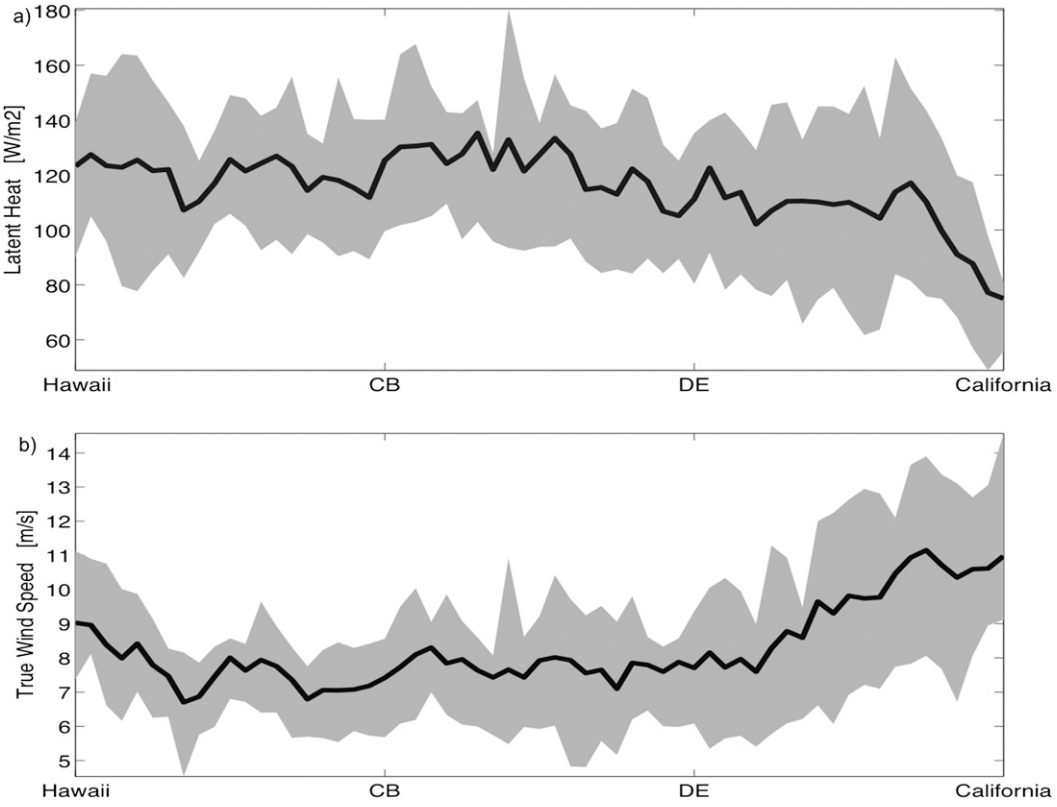

FIG. 12. The total mean (a) surface latent heat flux and (b) surface wind speed along the normalized path from California to Hawaii. Gray shaded region indicates interquartile range.

trend of LCL with increasing SST over the well-mixed MBL (Wyant et al. 1997; Sandu and Stevens 2011). The LCL height is more sensitive to the surface moisture than to the temperature. Thus, the increasing LCL height implies a gradual drying of the MBL, mainly due to the increasing entrainment rate with higher SST that is necessary to maintain the energy balance (Bretherton and Wyant 1997). During MAGIC, it is found that the LCL increase rapidly near DE (Fig. 11a), and the maximum increase in LCL with SST near DEs ranges from 122 to 369 m K^{-1}. The MAGIC observations suggest that this sudden dryness of the MBL is correlated with the entrainment of dryness above the inversion.

Figure 11b shows the mean $\Delta\theta_e$ (i.e., averaged over legs) over normalized distance from California to DE. The value of $\Delta\theta_e$ initially increased to near −2 K and then decreased to −6 K at DE. This decrease is mainly due to the large mean mixing ratio difference across the inversion (Fig. 11c). Plausible explanations for the drier conditions above the inversion are small displacements of the Hadley cell or cold outbreaks behind trailing cold fronts of midlatitude cyclones indicated by the increasing sea surface pressure from California to DE (Fig. 10b). The advection due to the large-scale circulation might also contribute. Meanwhile, the increase in both the potential temperature above the inversion (caused by the subsidence of the dry warm air) and that below (due to the increasing SST; Fig. 6g) explains the maintenance of the mean potential temperature difference across the inversion of near 6 K (Fig. 11d), which contributed less to the decrease $\Delta\theta_e$. The drop in $\Delta\theta_e$ east of the DE point increases (Fig. 12) the cloud-top entrainment instability and the entrainment rate (Deardorff 1980) and subsequently less moisture in the MBL. Consistent with the "deepening-warming mechanism" (Bretherton and Wyant 1997), our analysis concurs that entrainment plays a crucial role in inducing the MBL decoupling and the MAGIC observations also suggest that the dry warm air above the inversion might be an important trigger.

One would expect a dramatic increase of the LHF east of DE due to the dryness of the MBL; however, the mean surface latent heat was maintained around 120 W m^{-2} during that period (Fig. 12a). Therefore, the role of increasing latent heat fluxes in generating the systematic decoupling as suggested in the idealized model (Bretherton and Wyant 1997) is not captured by the MAGIC observations. The reduction of the mean surface wind speed from California to DE (Fig. 12b)

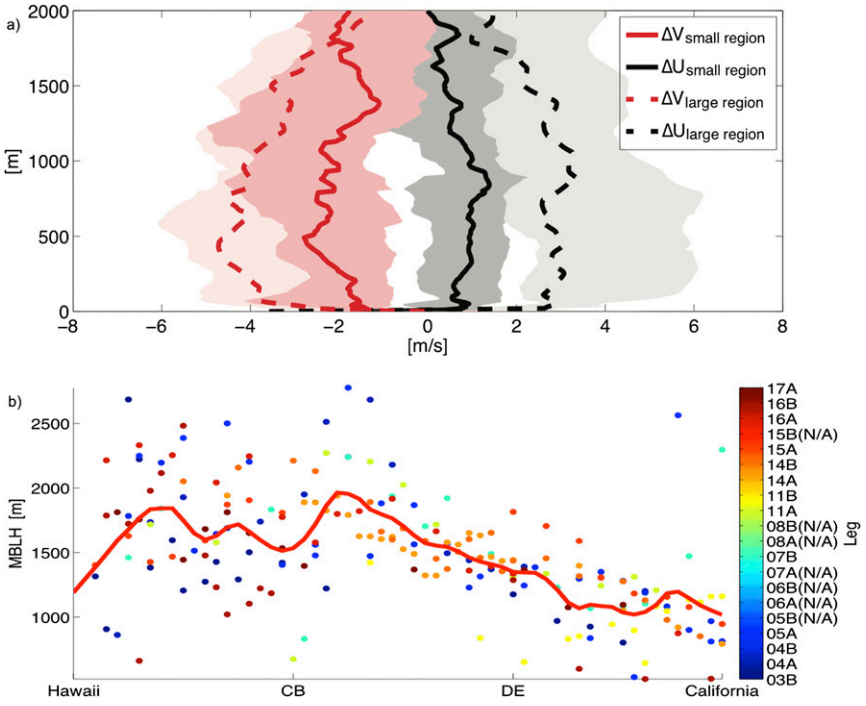

FIG. 13. (a) Profiles of medians of U wind difference of the composite U wind east of CB and that west of CB in the small region (solid black line) and in the large region (dashed black line); same for V wind difference in the small region (solid red line) and in the large region (dashed red line). The shaded area indicates interquartile range and (b) MBLH along normalized path from California to Hawaii.

regulates the increase of the LHF, when the ship moves from the edge to the center of the high pressure system (Fig. 10b). Thus, we conclude that LHF might be important in maintaining the systematic decoupling, but LHF does not play the dominant role in inducing decoupling in MAGIC, which is consistent with the conclusion of Jones et al. (2011).

Apart from the systematic decoupling, the weak decoupling ($\Delta z_i > 150$ m) east of DE is also investigated. Broad peaks of the frequency of occurrence of virga and drizzle were found east of DE, while these frequencies decreased to below 20% when MBL was decoupled (figures not shown). We found that 87% of these are associated with precipitation. We conclude that precipitation might play a role in inducing decoupling, but this decoupling is usually weak and not continuous; thus, precipitation did not show a dominant impact on systematic decoupling. Meanwhile, diurnal decoupling might also partly explain the weak decoupling east of DE since 73% of this occurred in the local daytime from 6:00 a.m. to 6:00 p.m.

2) POSSIBLE CONTROLLING FACTORS OF MBL CLOUD BREAKUP DURING MAGIC

Values of CF_{36} are typically high along the eastern part of the MAGIC transect (Fig. 10a), especially during the warm season (Fig. 6). The locations where CF_{108} drop to below 50% are usually close to CB (CF_{108} drops to below 15%), indicating the abrupt MBL cloud breakup (Fig. 10a) At the same time, CB is typically located on the west edge of high pressure systems (Fig. 10b), implying the role of synoptic interference in the observed MBL cloud breakup.

To further investigate this, we analyze the MBL wind profiles near the CB points. A clear synoptic-induced divergence pattern is found. Figure 13a shows median profiles of zonal (ΔU) and latitudinal (ΔV) wind difference of the composed U (V) wind east and west of CB in the small and large region. This small region is bounded by two days of radiosondes (~1600 km) surrounding CB while the large region refers to the whole transect. The profiles shown in Fig. 13a show little sensitivity to the details of the region selected to estimate the wind differences. The well-separated zonal and latitudinal wind differences around the CB indicate a systematic divergence in the MBL since the wind to the west of CB is more easterly ($\Delta U < 0\,\mathrm{m\,s^{-1}}$), and more southerly ($\Delta V > 0\,\mathrm{m\,s^{-1}}$) than that to the east. We interpret the east of CB wind pattern as the stable high pressure systems and the west of CB wind pattern as the signature of approaching midlatitude cyclone systems. Strong

TABLE A1. Departure and arrival times of each leg (date, time). All times are UTC.

	A		B	
	Depart LA	Arrive HI	Depart HI	Arrive LA
Leg00	11 Feb 2012, 1330	16 Feb 2012, 0900	17 Feb 2012, 0900	23 Feb 2012, 1500
Leg01			14 Sep 2012, 2320	20 Sep 2012, 1340
Leg02	22 Sep 2012, 1215	27 Sep 2012, 0550	28 Sep 2012, 0950	4 Oct 2012, 1420
Leg03	6 Oct 2012, 1130	11 Oct 2012, 0630	12 Oct 2012, 0800	18 Oct 2012, 1330
Leg04	20 Oct 2012, 1125	25 Oct 2012, 0615	26 Oct 2012, 0640	1 Nov 2012, 1320
Leg05	3 Nov 2012, 1750	8 Nov 2012, 1500	9 Nov 2012, 1730	15 Nov 2012, 1500
Leg06	17 Nov 2012, 1220	22 Nov 2012, 0730	24 Nov 2012, 1015	30 Nov 2012, 0120
Leg07	1 Dec 2012, 1330	6 Dec 2012, 0900	7 Dec 2012, 0820	13 Dec 2012, 1445
Leg08	15 Dec 2012, 1300	20 Dec 2012, 0830	22 Dec 2012, 0815	28 Dec 2012, 0000
Leg09*	29 Dec 2012, 1230	3 Jan 2013, 0700	5 Jan 2013, 0450	13 Jan 2013, 0335
Leg10	11 May 2013, 1120	16 May 2013, 0620	17 May 2013, 1630	23 May 2013, 1400
Leg11	25 May 2013, 1125	30 May 2013, 0630	31 May 2013, 1115	6 Jun 2013, 1330
Leg12	8 Jun 2013, 1125	13 Jun 2013, 0635	14 Jun 2013, 1635	20 Jun 2013, 1335
Leg13	22 Jun 2013, 1130	27 Jun 2013, 0745	28 Jun 2013, 1730	3 Jul 2013, 2310
Leg14	7 Jul 2013, 1735	12 Jul 2013, 0650	13 Jul 2013, 1145	18 Jul 2013, 2315
Leg15	20 Jul 2013, 1200	25 Jul 2013, 0545	26 Jul 2013, 1310	1 Aug 2013, 1330
Leg16	3 Aug 2013, 1330	8 Aug 2013, 0540	9 Aug 2013, 1015	15 Aug 2013, 1430
Leg17	17 Aug 2013, 1830	22 Aug 2013, 1015	23 Aug 2013, 1715	29 Aug 2013, 1320
Leg18	31 Aug 2013, 1145	5 Sep 2013, 0635	6 Sep 2013, 1200	12 Sep 2013, 1340
Leg19	14 Sep 2013, 1225	19 Sep 2013, 0620	20 Sep 2013, 1120	26 Sep 2013, 1355
Leg20**	28 Sep 2013, 1135	3 Oct 2013, 0635	4 Oct 2013, 1005	10 Oct 2013, 1335

* During Leg09B the *Spirit* had its engines off for approximately 14 h on 6 and 7 Jan 2013; thus the trajectory will look abnormal for this time as the ship was drifting. Soon thereafter the entire ship, including the AMF2, was without power for approximately 1 h, and some instruments might not have resumed operation before the end of the leg. Data acquisition stopped 11 Jan 2013 for some instruments and 12 Jan 2013 for all instruments. After the *Spirit* arrived in port in Los Angeles after Leg09B, the AMF2 was removed from the ship (it was completely off the Spirit by 2100 UTC 13 Jan 2013) and placed in storage, where it remained until reinstallation on 9 May 2013.

** MAGIC instrumentation was being turned off and packed during Leg20 and all MAGIC instrumentation was removed from the *Spirit* by 2200 UTC 10 Oct 2013.

uplifting convergence in the east-approaching cyclones was compensated by the divergence nearby. The drop of the MBLH near CBs provides evidence of the compensating subsidence (Fig. 13b), which is absent in the idealized model with uniformed large-scale forcing. Moreover, the averaged mixing ratio difference above the inversion was nearly doubled in the small region (not shown). We conclude that the switch of the synoptic environment to the unstable cyclone system can rapidly break up the MBL cloud and drive vigorous Cu or deep convective clouds.

5. Summary and discussion

The MAGIC field campaign, with nearly 200 days of ship-based observations during 20 round trips along the 4000-km transect between California and Hawaii, provided an unparalleled opportunity to acquire data on properties of MBL clouds, precipitation, and thermodynamic structure. The measurements obtained during that campaign are used in this manuscript to examine the location and potential controlling factors of systematic MBL decoupling and Sc breakup.

MBL clouds were by far the most frequently observed cloud type during the MAGIC campaign. MBL clouds occurred more often during the warm season (Fig. 5), reflecting the importance of the strong warm-season large-scale Hadley cell (Xu and Cheng 2013). Among the different MBL cloud types, Sc was the dominant MBL cloud type and occurred more frequently during the warm season than during the cold season (Fig. 8b), while the occurrence of Cu was less strongly affected by subsidence and exhibited nearly the same behavior for both seasons (Fig. 8b).

The formation of Sc just below the inversion requires a shallow MBL with a strong inversion and a weak transition (Fig. 9), providing a greater opportunity to have well-mixed MBL conditions. In contrast, Cu and multilayer clouds are usually associated with a much stronger transition, implying a greater chance of decoupling in the MBL.

There was a high frequency of occurrence of precipitation throughout the campaign. However, the precipitation from the MBL clouds is weak and often evaporated well before reaching the ocean surface (Fig. 6e). EIS experienced a seasonal variation caused by that of θ_{700} (Fig. 7c) and

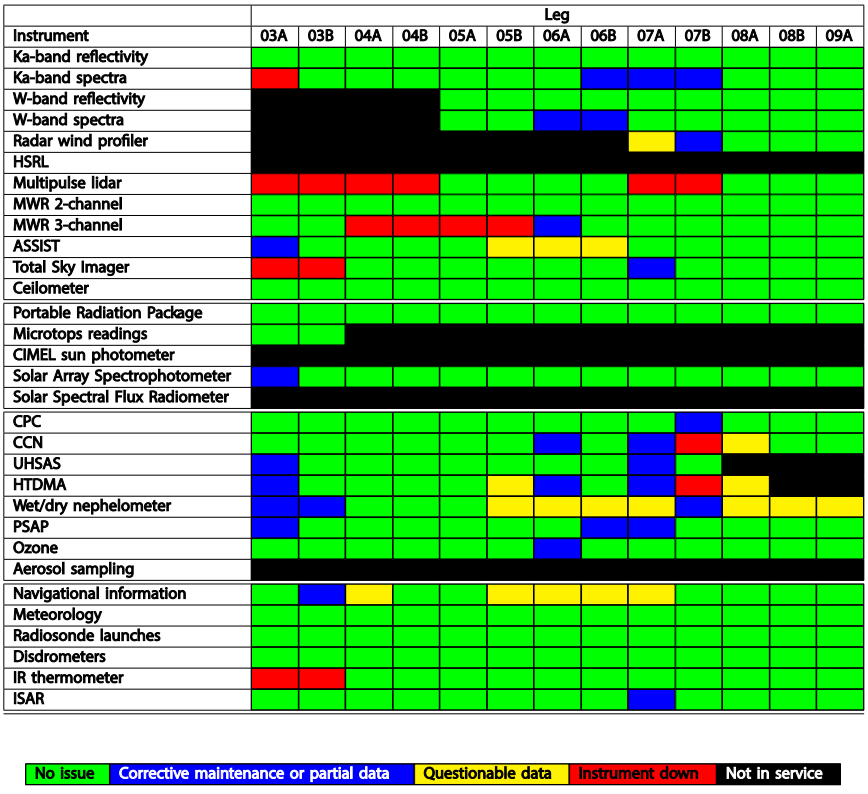

FIG. B1. MAGIC instrument status from Leg03A to Leg09B.

generally decreased due to the increasing SST. MBLH generally increased along the transect from California to Hawaii (Fig. 7). East of 135°W the spatial behavior of MBLH parallels that of the first cloud-top height (Figs. 5f and 6d), indicating the capped feature of the MBL.

The locations of MBL systematic decoupling are determined for individual legs. It is found that a threshold of $\Delta q > 1.5\,\mathrm{g\,kg^{-1}}$ separates the well-mixed profiles from the systematic decoupled ones (Fig. 5b). Compared to the threshold of $\Delta q > 0.5\,\mathrm{g\,kg^{-1}}$ found in VOCAL-REx (Jones et al. 2011), the MAGIC systematic decoupling showed much stronger moisture stratification below the inversion. Precipitation and diurnal circulation correlate well with the weak decoupling points between California and DEs, but neither of them plays a dominant role in the systematic decoupling.

A rapid increase of LCL height was found near DEs (Fig. 11a), indicating more rapid drying of the MBL. Correspondingly, the mean cloud-top instability showed a sudden increase, mainly due to the large mixing ratio difference across the inversion (Figs. 11b,c). These observations imply that the dry warm air from above the inversion is likely of great importance triggering the systematic decoupling. Consistent with the results in VOCAL-REx (Jones et al. 2011), LHF does not play the dominant role in inducing systematic decoupling in MAGIC. Meanwhile, the mixed layer cloud thickness during MAGIC did not correlate well with the systematic decoupling due to the sudden change of LCL near DEs, further implying that the strong entrainment was driven more by the cloud-top instability than by the in-cloud turbulence.

DEs nearly always occurred east of CBs (if present) (Fig. 10). MBL clouds tend to break up abruptly at a location that is typically on the west edge of high pressure systems (Fig. 10b). A change in synoptic pattern (i.e., different air mass) was often found near CB, which is associated with systematic divergence in the MBL. The divergence, together with downdrafts, compensated for the convergent uplifting in the approaching cyclones. We conclude that the cloud evolution in the idealized model seldom occurs in reality due to synoptic interference.

Acknowledgments. The MAGIC deployment was supported and undertaken by the U.S. Department of Energy (DOE) Atmospheric Radiation Measurement (ARM) Program Climate Research Facility. The

TABLE B1. Statistics (means and standard deviations) of MBL clouds macroscopic characteristics. The first cloud base, top, and thickness in the table refer to those of the lowest clouds.

Distance from California coast		100 km	500 km	1000 km	2000 km	3000 km	3600 km	4000 km
Cloud fractional coverage	Total	0.62 ± 0.44	0.69 ± 0.43	0.74 ± 0.41	0.62 ± 0.38	0.30 ± 0.38	0.33 ± 0.28	0.22 ± 0.28
	Cold	0.49 ± 0.47	0.54 ± 0.46	0.71 ± 0.44	0.54 ± 0.44	0.21 ± 0.27	0.29 ± 0.26	0.17 ± 0.27
	Warm	0.76 ± 0.37	0.88 ± 0.31	0.79 ± 0.40	0.71 ± 0.29	0.40 ± 0.48	0.38 ± 0.31	0.27 ± 0.29
First cloud base (km)	Total	0.51 ± 0.42	0.62 ± 0.34	0.98 ± 0.38	1.14 ± 0.28	1.05 ± 0.40	1.20 ± 0.43	1.11 ± 0.46
	Cold	0.85 ± 0.49	0.69 ± 0.47	1.04 ± 0.52	1.10 ± 0.20	1.09 ± 0.49	1.09 ± 0.46	1.17 ± 0.53
	Warm	0.27 ± 0.08	0.55 ± 0.15	0.92 ± 0.17	1.18 ± 0.36	1.00 ± 0.26	1.32 ± 0.39	1.04 ± 0.37
First cloud top (km)	Total	0.89 ± 0.75	0.91 ± 0.42	1.19 ± 0.28	1.39 ± 0.28	1.20 ± 0.47	1.43 ± 0.47	1.24 ± 0.35
	Cold	1.36 ± 0.90	1.02 ± 0.56	1.17 ± 0.35	1.39 ± 0.24	1.19 ± 0.57	1.31 ± 0.52	1.15 ± 0.31
	Warm	0.48 ± 0.13	0.80 ± 0.16	1.20 ± 0.19	1.39 ± 0.33	1.23 ± 0.34	1.57 ± 0.39	1.33 ± 0.39
First cloud thickness (km)	Total	0.35 ± 0.39	0.27 ± 0.22	0.23 ± 0.15	0.23 ± 0.16	0.19 ± 0.15	0.17 ± 0.13	0.24 ± 0.18
	Cold	0.60 ± 0.51	0.30 ± 0.30	0.18 ± 0.11	0.25 ± 0.16	0.18 ± 0.16	0.15 ± 0.15	0.26 ± 0.19
	Warm	0.18 ± 0.14	0.24 ± 0.11	0.27 ± 0.17	0.21 ± 0.16	0.21 ± 0.15	0.21 ± 0.08	0.21 ± 0.17

Means and standard deviations of the cloud macroscopic properties at different locations along the MAGIC transect (100, 500, 1000, 2000, 3000, 3600 and 4000 km from the coast of California) for all applicable MAGIC legs (Leg3–8, Leg11, Leg14–17). Data during each leg are binned to a uniform great circle route with 36-km resolution.

current research was supported by the DOE Atmospheric System Research (ASR) Program (Office of Science, OBER). ERL was supported by the ASR Program under Contract DE-AC02-98CH10886. Data used for the analyses were downloaded from the ARM archive (www.arm.gov) except for the MARMET and MARFLUX data, which were provided by Dr. Michael Reynolds of RMR Co. We thank David Painemal of NASA Langley Research Center for providing surface cloud condensation nuclei (CCN) data. We acknowledge the team of scientists and technicians who made this work possible by collecting the data and maintaining the instruments, and especially Horizon Lines and the captain and crew of the Horizon *Spirit* for their hospitality. Special thanks go to the cloud research group at McGill University

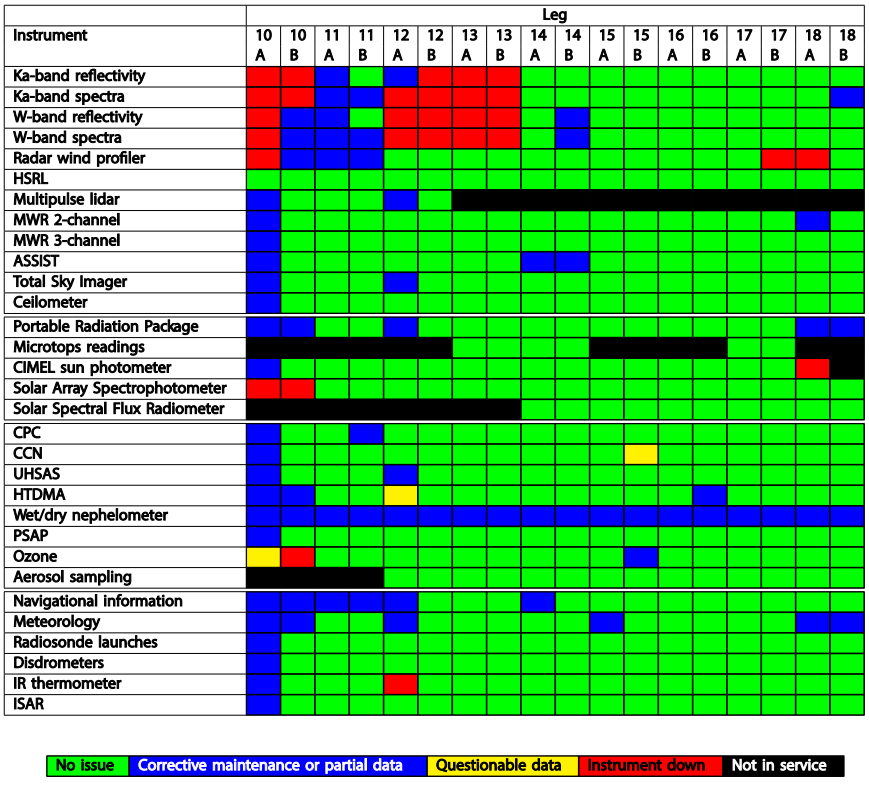

FIG. B2. MAGIC instrument status from Leg10A to Leg18B.

(www.clouds.mcgill.ca) for their helpful comments and constructive criticism.

APPENDIX A

MAGIC Campaign Schedule

Departure and arrival times of each leg are listed in Table A1.

APPENDIX B

MAGIC Instrument Status

a. Instrument status table Leg03A to Leg09B

The first leg with MAGIC instrumentation was Leg01B during which the ISAR was installed. (MAGIC instrument status from Leg03A to Leg09B is shown in Figure B1, for cloud characteristic statistics see Table B1). During Leg02A and Leg02B, for which instrument status designations are not listed, the radars and other instruments were being set up; some collected data during these legs. During Leg03 most of the instruments were up and collecting data. On Leg09B, the instruments were without power for extended times and were being shut down. The instruments were removed from the ship after Leg09B from January 2013 until May 2013.

b. Instrument status table Leg10A to Leg18B

MAGIC instruments were redeployed during Leg10A, and the campaign continued until the end of Leg20B. (MAGIC instrument status from Leg10A to Leg18B is shown in Figure B2.) The technicians did not report instrument status designations for Leg19A and Leg19B, but these were probably similar to those for Leg18B. During Leg20A and Leg20B the instruments were being turned off, so few data were collected during these legs (although sonde launches occurred on Leg20A, meteorological data were collected until the ship returned to port, and both radars were operating for most of the two legs).

REFERENCES

Albrecht, B. A., 1984: A model study of downstream variations of the thermodynamic structure of the trade winds. *Tellus,* **36A,** 187–202, doi:10.1111/j.1600-0870.1984.tb00238.x.

——, D. A. Randall, and S. Nicholls, 1988: Observations of marine stratocumulus clouds during FIRE. *Bull. Amer. Meteor. Soc.,* **69,** 618–626, doi:10.1175/1520-0477(1988)069<0618:OOMSCD>2.0.CO;2.

——, C. S. Bretherton, D. Johnson, W. H. Scubert, and A. S. Frisch, 1995a: The Atlantic Stratocumulus Transition Experiment—ASTEX. *Bull. Amer. Meteor. Soc.,* **76,** 889–904, doi:10.1175/1520-0477(1995)076<0889:TASTE>2.0.CO;2.

——, M. P. Jensen, and W. J. Syrett, 1995b: Marine boundary layer structure and fractional cloudiness. *J. Geophys. Res.,* **100** (D7), 14 209–14 222, doi:10.1029/95JD00827.

Augstein, E., H. Schmidt, and F. Ostapoff, 1974: The vertical structure of the atmospheric planetary boundary layer in undisturbed trade winds over the Atlantic Ocean. *Bound.-Layer Meteor.,* **6,** 129–150, doi:10.1007/BF00232480.

Bohren, C., and B. Albrecht, 1998: *Atmospheric Thermodynamics.* Oxford University Press, 402 pp.

Bretherton, C. S., and R. Pincus, 1995: Cloudiness and marine boundary layer dynamics in the ASTEX Lagrangian experiments. Part I: Synoptic setting and vertical structure. *J. Atmos. Sci.,* **52,** 2707–2723, doi:10.1175/1520-0469(1995)052<2707:CAMBLD>2.0.CO;2.

——, and M. C. Wyant, 1997: Moisture transport, lower-tropospheric stability, and decoupling of cloud-topped boundary layers. *J. Atmos. Sci.,* **54,** 148–167, doi:10.1175/1520-0469(1997)054<0148:MTLTSA>2.0.CO;2.

Deardorff, J., 1980: Cloud top entrainment instability. *J. Atmos. Sci.,* **37,** 131–147, doi:10.1175/1520-0469(1980)037<0131:CTEI>2.0.CO;2.

Fairall, C. W., E. F. Bradley, D. P. Rogers, J. B. Edson, and G. S. Young, 1996: Bulk parameterization of air–sea fluxes for Tropical Ocean–Global Atmosphere Coupled Ocean–Atmosphere Response Experiment. *J. Geophys. Res.,* **101** (C2), 3747–3764, doi:10.1029/95JC03205.

Heck, P. W., B. J. Byars, D. F. Young, P. Minnis, and E. F. Harrison, 1990: A climatology of satellite derived cloud properties over marine stratocumulus regions. Preprints, *Conf. on Cloud Physics,* San Francisco, CA, Amer. Meteor. Soc., J1–J7.

Hildebrand, P. H., and R. Sekhon, 1974: Objective determination of the noise level in Doppler spectra. *J. Appl. Meteor.,* **13,** 808–811, doi:10.1175/1520-0450(1974)013<0808:ODOTNL>2.0.CO;2.

Jones, C. R., C. S. Bretherton, and D. Leon, 2011: Coupled vs. decoupled boundary layers in VOCALS-REx. *Atmos. Chem. Phys.,* **11,** 7143–7153, doi:10.5194/acp-11-7143-2011.

Karlsson, J., G. Svensson, S. Cardoso, J. Teixeira, and S. Paradise, 2010: Subtropical cloud-regime transitions: Boundary layer depth and cloud-top height evolution in models and observations. *J. Appl. Meteor. Climatol.,* **49,** 1845–1858, doi:10.1175/2010JAMC2338.1.

Klein, S. A., and D. L. Hartmann, 1993: The seasonal cycle of low stratiform clouds. *J. Climate,* **6,** 1587–1606, doi:10.1175/1520-0442(1993)006<1587:TSCOLS>2.0.CO;2.

Kollias, P., E. Clothiaux, M. Miller, B. Albrecht, G. Stephens, and T. Ackerman, 2007: Millimeter-wavelength radars: New frontier in atmospheric cloud and precipitation research. *Bull. Amer. Meteor. Soc.,* **88,** 1608–1624, doi:10.1175/BAMS-88-10-1608.

Krueger, S. K., G. T. McLean, and Q. Fu, 1995: Numerical simulation of the stratus-to-cumulus transition in the subtropical marine boundary layer. Part I: Boundary-layer structure. *J. Atmos. Sci.,* **52,** 2839–2850, doi:10.1175/1520-0469(1995)052<2839:NSOTST>2.0.CO;2.

Lewis, E. R., and Coauthors, 2012: MAGIC: Marine ARM GPCI Investigation of Clouds. DOE/SC-ARM-12-020, U.S. Department of Energy, 12 pp.

Lilly, D. K., 1968: Models of cloud-topped mixed layers under a strong inversion. *Quart. J. Roy. Meteor. Soc.,* **94,** 292–309, doi:10.1002/qj.49709440106.

Lohmann, U., and J. Feichter, 2005: Global indirect aerosol effects: A review. *Atmos. Chem. Phys.,* **5,** 715–737, doi:10.5194/acp-5-715-2005.

Matrosov, S. Y., 2007: Potential for attenuation-based estimations of rainfall rate from CloudSat. *Geophys. Res. Lett.,* **34,** L05817, doi:10.1029/2006GL029161.

Moran, K. P., B. E. Martner, M. J. Post, R. A. Kropfli, D. C. Welsh, and K. B. Widener, 1998: An unattended cloud-profiling radar for use in climate research. *Bull. Amer. Meteor. Soc.,* **79,** 443–455, doi:10.1175/1520-0477(1998)079<0443:AUCPRF>2.0.CO;2.

Rémillard, J., P. Kollias, E. Luke, and R. Wood, 2012: Marine boundary layer cloud observations in the Azores. *J. Climate,* **25,** 7381–7398, doi:10.1175/JCLI-D-11-00610.1.

Sandu, I., and B. Stevens, 2011: On the factors modulating the stratocumulus to cumulus transitions. *J. Atmos. Sci.,* **68,** 1865–1881, doi:10.1175/2011JAS3614.1.

Teixeira, J., and Coauthors, 2011: Tropical and subtropical cloud transitions in weather and climate prediction models: The GCSS/WGNE Pacific Cross-Section Intercomparison (GPCI). *J. Climate,* **24,** 5223–5256, doi:10.1175/2011JCLI3672.1.

Tiedtke, M., W. A. Hackley, and J. Slingo, 1988: Tropical forecasting at ECMWF: The influence of physical parameterization on the mean structure of forecasts and analyses. *Quart. J. Roy. Meteor. Soc.,* **114,** 639–664, doi:10.1002/qj.49711448106.

Wang, S., B. A. Albrecht, and P. Minnis, 1993: A regional simulation of marine boundary layer clouds. *J. Atmos. Sci.,* **50,** 4022–4043, doi:10.1175/1520-0469(1993)050<4022:ARSOMB>2.0.CO;2.

Widener, K., N. Bharadwaj, and K. Johnson, 2012: Ka-band ARM Zenith Radar (KAZR) instrument handbook. DOE Office of Science Atmospheric Radiation Measurement (ARM) Program, 19 pp.

Wood, R., 2012: Stratocumulus clouds. *Mon. Wea. Rev.,* **140,** 2373–2423, doi:10.1175/MWR-D-11-00121.1.

——, and C. S. Bretherton, 2004: Boundary layer depth, entrainment, and decoupling in the cloud-capped subtropical and tropical marine boundary layer. *J. Climate,* **17,** 3576–3588, doi:10.1175/1520-0442(2004)017<3576:BLDEAD>2.0.CO;2.

——, and ——, 2006: On the relationship between stratiform low cloud cover and lower-tropospheric stability. *J. Climate,* **19,** 6425–6432, doi:10.1175/JCLI3988.1.

——, and Coauthors, 2011: The VAMOS Ocean–Cloud–Atmosphere–Land Study Regional Experiment (VOCALS-REx): Goals, platforms, and field operations. *Atmos. Chem. Phys.,* **11,** 627–654, doi:10.5194/acp-11-627-2011.

Wyant, M. C., C. S. Bretherton, H. A. Rand, and D. E. Stevens, 1997: Numerical simulations and a conceptual model of the subtropical marine stratocumulus to trade cumulus transition. *J. Atmos. Sci.,* **54,** 168–192, doi:10.1175/1520-0469(1997)054<0168:NSAACM>2.0.CO;2.

Xu, K.-M., and A. Cheng, 2013: Evaluating low cloud simulation from an upgraded multiscale modeling framework model. Part I: Sensitivity to spatial resolution and climatology. *J. Climate,* **26,** 5717–5740, doi:10.1175/JCLI-D-12-00200.1.

Yin, B., and B. A. Albrecht, 2000: Spatial variability of atmospheric boundary layer structure over the eastern equatorial Pacific. *J. Climate,* **13,** 1574–1592, doi:10.1175/1520-0442(2000)013<1574:SVOABL>2.0.CO;2.